

REMOTE SENSING OF CRITERIA AND NON-CRITERIA POLLUTANTS EMITTED IN THE EXHAUST OF ON-ROAD VEHICLES

Marc M. Baum¹, Eileen S. Kiyomiya¹, Sasi Kumar¹, Anastasios M. Lappas¹,
and Harry C. Lord III²

¹Department of Chemistry, Oak Crest Institute of Science, 13300 Brooks Dr, Suite B, Baldwin Park, CA 91706, ²Air Instruments & Measurements, Inc, 13300 Brooks Dr, Suite A, Baldwin Park, CA 91706

INTRODUCTION

Emissions from mobile sources are well known to play a central role in urban air pollution (photochemical smog formation, violation of CO and ozone O₃ standards, and aerosol formation). The Clean Air Act Amendments of 1990 call for auto makers to reduce tailpipe emissions of hydrocarbons and nitrogen oxides by 35 % and 60 % respectively. CO emission standards of no more than 10 g mi⁻¹ for light duty motor vehicles have also been set. Additional emission reductions for all three pollutants have been scheduled for the early 2000s. Data collected from remote sensing studies of large fleets of in-use vehicles indicate that approximately half of CO, hydrocarbon (THC), and NO emissions are generated by less than 10% of vehicles. Moreover, remote sensing data suggest that fleet dynamometer testing significantly underestimates tailpipe emissions, and contribute to errors in model predictions (e.g., U.S. EPA's MOBILE4). A knowledge of the chemical composition of the exhaust plume emitted by on-road vehicles on a car-by-car basis therefore is essential when developing effective pollution abatement strategies, and in helping meet Clean Air Act objectives.

EXPERIMENTAL

A remote sensor incorporating UV-vis and IR spectrometers in conjunction with an innovative optical design has been developed. The instrument was used to non-invasively measure over 20 pollutants in the exhaust of 19 in-use vehicles powered by a range of fuels – reformulated Phase II gasoline, diesel, compressed natural gas, and methanol blended with 15% gasoline. CO₂, CO, aldehydes, aliphatic and speciated aromatic hydrocarbons were identified along with NO_x, determined as the sum of NO, NO₂; N₂O and HONO was also measured, although their levels were typically below the instrument's detection limit.

RESULTS AND DISCUSSION

The results are summarized in Table 1 below.

Table 1. Effect of fuel type on vehicle exhaust emissions.

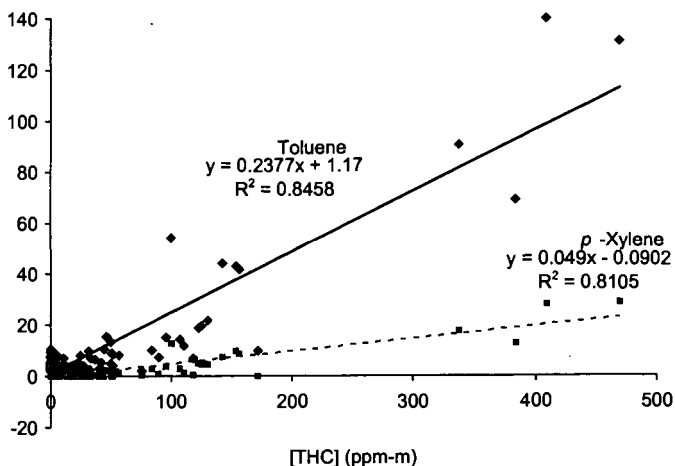
| Fuel | [HC] _{mean} (ppm) | [CO] _{mean} (%) | [NO] _{mean} (ppm) | [NH ₃] _{mean} (ppm) |
|----------|-------------------------------|-----------------------------|-------------------------------|---|
| Gasoline | 126.5 | 1.92 | 475.6 | 317.0 |
| Diesel | 50.1 | 0 | 934.6 | 0.0 |
| CNG | 55.8 | 0.34 | 2041.3 | 12.1 |
| M-85 | 25.5 ^a | 2.01 | 0.0 | 438.5 |

^aMeasured as methanol.

NH₃ levels in vehicle exhaust are reported for the first time on a car-by-car basis. The exhaust from gasoline- and methanol-powered cars was found to contain elevated levels of NH₃, in some cases over 1000 ppm, despite near stoichiometric air-to-fuel ratios, and were often significantly higher than corresponding NO levels. Catalyst efficiency is discussed as a function of NH₃ and NO concentrations in the exhaust of vehicles operating "cold" and "hot". In some of the tested vehicles, the three-way catalysts showed high reduction activity, but poor selectivity resulting in the formation of NH₃, and possibly other nitrogen-containing products other than N₂.

Remote sensing was also performed on the exhaust emissions from over 2,100 vehicles as they drove up a freeway on-ramp. Criteria pollutants, CO, THC, and NO, were found to follow a γ -distribution and agreed with data from previous remote sensing studies using a different technology; over half the total pollutant emissions are from 10 % of the fleet. Optical densities of the two principal aromatic hydrocarbon components of gasoline, toluene and xylene, were found to correlate well with THC measurements (Fig. 1), despite the fact that the measurements were made by different techniques; UV (aromatics) and IR (THC) absorption spectroscopy.

Figure 1.



Note: concentrations are shown as column densities, not as levels in undiluted exhaust.

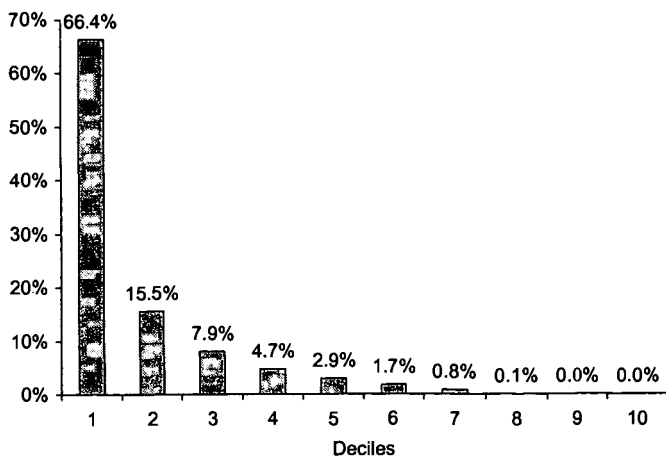
Emission rates of CO, THC, NO, toluene and xylene are shown in Table 2 below.

Table 2.

| Pollutant X | Mean [X]/[CO ₂] | Max. (ppm) | <i>E_m</i> (mg/km) |
|-----------------|--------------------------------|---------------|---------------------------------|
| NO | 0.00381 | 4963 | 940 |
| NH ₃ | 0.00056 | 3934 | 138 |
| Toluene | 0.00018 | 1620 | 44 [†] |
| p-Xylene | 0.000037 | 350 | 9 [†] |

[†]Based on relationship to THC emissions.

Figure 2.



SUMMARY AND CONCLUSIONS

For the first time, remote sensing was used to measure NH₃ directly in the exhaust plume emitted by on-road vehicles. It was shown that 66.4 % of the emitted NH₃ was produced by 10 % of the fleet as illustrated by the decile plot given in Figure 2; the first decile represents the fraction of the total analyte produced by the 10 % dirtiest fraction of the measured vehicle fleet, and so on.

Mean NH_3 emission rates were calculated at 138 mg km^{-1} , nearly twice as high as previous estimates. However, it is expected that NH_3 generation in three-way catalysts is highly dependent on driving conditions and, therefore, NH_3 emission rates will probably vary as a function of the remote sensing test site. These observations could have significant implications on the formation of ammonium nitrate aerosol and on the acid-neutralizing capacity of urban air masses and NH_3 emissions from motor vehicles may need to be addressed in future amendments of the Clean Air Act.

ACKNOWLEDGEMENTS

We would like to acknowledge cooperation of the Gas Company and Rio Hondo in supplying us with natural gas-powered test vehicles and support, as well as CalTrans for issuing a permit in haste.

This research was supported by the South Coast Air Quality Management District under contract No. AB2766/96028. We gratefully acknowledge the valuable assistance provided by this program, as well as the loan of the M85 vehicle.

The statement and conclusions in this paper are those of the contractor and not necessarily those of the Mobile Source Air Pollution Review Committee (MSRC) or the South Coast Air Quality Management District (SCAQMD). The mention of commercial products, their sources or their uses in connection with material reported herein is not to be construed as either an actual or implied endorsement of such products.

CHARACTERIZATION OF FLY ASH CARBONS DERIVED DUE TO THE IMPLEMENTATION OF NO_x CLEAN AIR ACT AMENDMENTS

M. Mercedes Maroto-Valer¹, Darrell N. Taulbee² and James C. Hower²

¹The Energy Institute, The Pennsylvania State University,
405 Academic Activities Building, University Park, PA-16802

²University of Kentucky - Center for Applied Energy Research, 2540 Research Park Drive,
Lexington, KY-40511

Keywords: NO_x Clean Air Act Amendments, fly ash carbons, properties.

One of the more extensively used approaches for meeting the Title IV of the 1990 Clean Air Act Phase-I has been the installation of low-NO_x burners. Although these technologies have been proven effective in reducing NO_x emissions, they have also resulted in an increase in the concentration of unburned carbon in the fly ash. This has restricted the principal use of ash in the cement industry, since the unburned carbon tends to adsorb the air-entrainment admixtures (AEAs), that are added to the cement to prevent crack formation and propagation. However, very little is known about the properties of fly ash carbons and any information regarding their properties is watched closely by the utility industry. Accordingly, the work reported here represents the first characterization of the bulk properties of unburned carbon concentrates that have been isolated to purities up to 86% by using density gradient centrifugation. The density of like carbon forms isolated from two fly ashes appears to be quite similar, regardless of the source of the fly ash. The H/C atomic ratios are ~ 0.028-0.016, indicating a high degree of condensation. The BET surface areas are relatively low, ranging from 10 to 60 m²/g, and most of the pores are in the mesopore range (2-50 nm in width). For both series of fly ash samples, the surface area was found to increase linearly with increasing particle density.

INTRODUCTION

The Environmental Protection Agency (EPA) issued, under Title IV of the 1990 Clean Air Act Amendment, a two-phase strategy to reduce NO_x emissions from coal-fired utility boilers. Phase I took effect on January 1996 and promulgated that emissions levels from Group-1 boilers should be reduced by over 400,000 tons/year between 1996-1999 [1]. Group-1 is formed by dry-bottom wall-fired boilers and tangentially fired boilers and their emissions levels were reduced to 0.50 and 0.45 lb NO_x / MM Btu, respectively. Phase II, that began last January, will achieve an additional reduction of ~ 900,000 tons of NO_x annually. Phase II has lowered the emission levels for Group-1 boilers to 0.46 - 0.40 lb NO_x / MM Btu, and established limits for Group-2 boilers, that include cell, cyclones, wet bottoms and vertically fired boilers to levels down to 0.68, 0.86, 0.84, and 0.80 lb NO_x / MM Btu, respectively [2]. Nevertheless, Phase II regulation has been dormant during a litigation process that was originated by eight upwind states and a number of utilities, that sued EPA's authority to issue the rule [3]. However, a federal appeals court has recently upheld EPA's rule and the administration has requested to reactivate the rule. It is expected that facilities in 19 states could be affected by the implementation of this regulation.

One of the more extensively used approaches for meeting the Title IV of the 1990 Clean Air Act Phase-I has been the retrofitting of several hundred existing boilers with low-NO_x burners. Furthermore, EPA has projected that around 85-90% of the boilers in both Group-1 and 2 could meet the required NO_x reduction levels by installing low-NO_x burners [2], leaving other technologies, such as Selective Catalytic Reduction (SCR) and Selective Non-Catalytic Reduction (SNCR) suitable complimentary approaches to meet the required NO_x reduction levels. The installation of low-NO_x burners changes the flame-temperature profile as well as the flame chemistry since, in essence, a hot oxygen-rich flame is replaced by a cooler and longer, fuel-rich flame. While these modifications have proven effective in reducing NO_x emissions, they have also resulted in a lower combustion efficiency, leading to an increase in the concentration of unburned carbon in the fly ash [4]. Although the unburned carbon is known to preclude the use of fly ash in the cement industry, very little is known about the properties of this material and any information regarding its properties is watched closely by the utility industry.

It is generally known that the ASTM LOI specification is not sufficient to identify the suitability of a fly ash for the cement industry, since this criterion only gives a rough approximation to the carbon content of a sample and does not directly correlate with the capacity to adsorb air entrainment admixtures (AEAs), that are added to the cement to prevent crack formation and propagation [5,6]. In fact, prior petrographic examinations of a number of high-carbon fly ashes have shown that the unburned carbon is not visually uniform [7]. Three microscopically distinct carbon types have been identified: (i) inertinite particles, which appear to have been entrained from the combustor prior to melting or combustion; (ii) isotropic coke; and (iii) anisotropic coke, the latter two being extensively reacted particles, which appear to have passed through a molten stage [7,8]. The above particle types can be further subdivided according to particle shape, pore volume and wall thickness [9]. Although several studies have been conducted on the characterization of

whole fly ash samples [5,6], very little is known about the relative properties of the three carbon types, as their isolation is not a trivial task. For example, it is not known whether a fly ash that contains mainly inertinite has the same capacity to absorb air entrainment agents as an otherwise equivalent fly ash containing predominantly isotropic carbon. If in fact the capacity to absorb air entrainment agents varies substantially for the differing forms of unburned carbon, it may be possible to establish a criterion based on the relative properties of the differing carbon types to identify suitable fly ashes for the cement industry, regardless of their LOI value. Accordingly, this work presents the first characterization of these differing forms of unburned carbon, that have been previously separated by Density Gradient Centrifugation (DGC). The authors have successfully developed a method to isolate the three differing forms of unburned carbon [10,11]. The methodology used includes a preliminary triboelectrostatic enrichment or acid digestion, followed by DGC with a high-density lithium polytungstate media (2.85 g cm^{-3} max). Two fly ashes, identified as Dale and WEPCO, obtained from different power plants, were separated by the above procedure. In this work, the highest purity fractions from these separations were extensively analyzed by several analytical techniques, including elemental and surface area analyses.

EXPERIMENTAL

Two fly ashes, identified as Dale and WEPCO, were examined in this study. For the Dale sample, approximately 12 kg of fly ash were collected from the mechanical precipitators of a 70 MW boiler (Dale unit #3) operated by Eastern Kentucky Power. The WEPCO (Wisconsin Electric Power Co.) sample was collected from the electrostatic precipitators of a 136 MW unit at Valley Power Station. A series of preliminary enrichments were conducted to increase the amount of carbon in the ash and thereby, minimize the number of DGC runs. These steps included an initial screening of the sample with a 140 mesh sieve ($106 \mu\text{m}$), with the 140+ fraction being triboelectrostatically separated to obtain a sample (Dale-TES) with an inorganic matter content below 10 %. This carbon-enriched fraction was then used as the feed for subsequent DGC separations. The WEPCO (Wisconsin Electric Power Co.) sample was processed directly through the triboelectrostatic separator without the initial screening step. Again, the carbon-enriched fraction (WEPCO-TES) was used as the feed material in a subsequent DGC separation, using a lithium heteropolytungstate high-density media. Details of the DGC separation procedure can be found elsewhere [10, 11].

Petrographic analyses of the fly ash parent samples and DGC fractions were performed on epoxy-bound polished pellets using oil-immersion objectives at a final magnification of 500-625x. The elemental analyses were carried out on a Leco CHN-600 analyzer. The porosity of the samples was determined via N_2 adsorption isotherms at 77K using a Quantachrome adsorption apparatus, Autosorb-1 Model ASiT. The BET surface areas were calculated using the adsorption points at the relative pressures (P/P_0) 0.05 - 0.25. The values reported were corrected to a mineral-free basis using the $6 \text{ m}^2/\text{g}$ surface area measured for the 2.5 g cm^{-3} density fraction of the fly ash and the TGA-derived inorganic contents for the respective density fractions [11]. The total pore volume, V_{TOT} , was calculated from the amount of vapor adsorbed at the relative pressure of 0.95. The mesopore (pores 2-50 nm in width) volume was calculated using the BJH equation.

RESULTS AND DISCUSSION

Purities and densities of the fraction separated by DGC The petrographic data for the Dale and WEPCO parent samples and the carbon-enriched DGC feed samples (Dale-TES and WEPCO-TES) are presented in Table 1 on a volume % basis. The parent Dale fly ash contained approximately 64% glass, while its -140 fraction had ~91% glass. The glass content was reduced to ~59% in the +140 mesh fraction and to less than 10% following the triboelectrostatic separation. The predominant carbon type is anisotropic coke. The relative proportions of the three carbon types in the parent and the beneficiated Dale samples are very similar, with the exception of a slight reduction in inertinites in the +140 fraction and resultant subsamples. However, even these minor changes were not statistically significant as they stay within the experimental error of the petrographic measurements ($\pm 5\%$). The WEPCO sample was selected for this study for two reasons. First, to determine if like carbon forms exhibited the same densities regardless of the source of the fly ash. Second, the WEPCO sample contained a higher proportion of isotropic relative to anisotropic coke, which, assuming like carbon forms do in fact have the same density, should be reflected by the weight recovery curve. For the WEPCO sample, a similar reduction in the glass content was observed after the triboelectrostatic separation, going from ~60% to ~10% (Table 1). The predominant carbon form in the WEPCO sample is isotropic coke. However, there seems to be somewhat higher beneficiation of the anisotropic carbon, compared to the other carbon types, during the triboelectrostatic separation. Nevertheless, this difference stays within the experimental error. Whether triboelectrostatic separations truly discriminate certain carbon types has not been fully investigated.

Figure 1 shows the petrographic composition for all the density fractions recovered for the WEPCO-TES fractions. The highest enrichment is for inertinites (densities $< 1.60 \text{ g cm}^{-3}$ with purity of ~85%) and is similar to that found for Dale-TES. Isotropic coke particles partitioned predominantly at densities $\sim 1.725\text{-}1.750 \text{ g cm}^{-3}$, similar to the Dale-TES sample, but presented higher purities (79% cf. 72%), due in part to the higher proportion of isotropic carbon present in the parent sample, as well as the smaller particle size and lower frequency of mixed particles. Anisotropic coke particles maximized at similar densities and purities to those observed for the Dale separations. The higher density fractions are dominated by inorganic particles, with spinel being the most dense mineral. This is consistent with the values reported for spinel and glass minerals, where the former has a specific gravity of 3.55 g cm^{-3} , while the latter is $\sim 2.50 \text{ g cm}^{-3}$. Previous centrifugal separations have also reported a higher partition of non-glassy particles, consisting primarily of iron oxides, at densities $> 2.40 \text{ g cm}^{-3}$ [12, 13].

The petrographic analysis of the three highest purity carbon-type fractions from each separation along with the density range over which these highest purity fractions were recovered are also shown in Table 1. After DGC separation, enrichments ranged up to 85.5 vol% inertinite in the WEPSCO separation, up to 78.5 vol% isotropic coke for the WEPSCO separation, and up to 76 vol% anisotropic coke in the Dale and WEPSCO carbon-enriched separations (Table 1). Note that the differences in the fraction number in which the highest purities were obtained for the three separations is due to changes made in the cut-point densities for the three separations and not necessarily to differences in particle density. Maximum purities were obtained at similar densities for both samples. That is, inertinite purity maximizes in the lowest density fractions ($<1.65 \text{ g cm}^{-3}$), isotropic-coke purity maximizes between 1.72 and 1.78 g cm^{-3} , and anisotropic-coke purity maximizes between 1.88 and 1.94 g cm^{-3} . Thus, these data indicate that the density of the three unburned carbon types to be similar in these two fly ash samples despite the differences in the starting coal or the utility combustor from which they were derived.

Elemental analyses and atomic ratios CHN analyses were carried out only on the Dale carbon-enriched separation samples. The results of these analyses conducted on the DGC feed and selected higher-purity carbon-type fractions are shown in Table 2. The elemental analyses show that the three types of unburned carbon consist primarily of C, while the H content is below 0.23. The H/C atomic ratios range between 0.028 to 0.016, indicating a high degree of condensation. Any trends that may be present in the hydrogen data and atomic H/C ratios are masked by the error of the analysis stemming from the very low hydrogen concentrations coupled with potential interferences from adsorbed moisture. However, there does appear to be a correlation between nitrogen concentration and carbon type (or fraction density), where higher nitrogen concentrations and N/C atomic ratios are associated with increasing density. In addition, there also appears to be a higher level of oxygen in the isotropic coke particles (fraction nos. 5 and 6). FT-IR spectra were conducted on selected density fractions in an effort to determine if the isotropic-rich fractions were measurably greater in carbonyl (C=O) functional groups, the only oxygen functionality to which infra-red analysis would be sufficiently sensitive to detect, but these analysis were inconclusive. Nevertheless, similar trend has been found previously by other authors, where fly ashes with predominant isotropic coke presented higher oxygen levels than ashes with predominantly anisotropic coke [5]. In this previous study, diffuse reflectance FT-IR was also used, but again this technique did not detect carbonyl functional groups, implying that the oxygen was most likely bound as heterocyclic compounds. The reason for these trends in the nitrogen and oxygen levels is unclear, but these distinctive concentrations as a function of unburned carbon type may be reflected in differences in adsorption properties.

Surface area, pore volume and adsorption properties The N_2 adsorption isotherms of all the samples investigated were Type II according to the BDDT classification and they are typical for nonporous or macroporous adsorbents, on which unrestricted monolayer-multilayer adsorption can occur. BET surface area (N_2 at 77K) measurements were carried out on the Dale and WEPSCO carbon-enriched separation samples. The surface areas are relatively low, ranging from 10 to $60 \text{ m}^2/\text{g}$. The WEPSCO parent fly ash and subsequent subsamples present slightly higher surface areas than those observed for their counterparts of the Dale separations. For example, the inertinite fraction derived from WEPSCO fly ash has a surface area of $25 \text{ m}^2/\text{g}$, compared to only $15 \text{ m}^2/\text{g}$ for the inertinite fraction derived from Dale fly ash. For both series of fly ash samples, the surface area was found to increase linearly as a function of particle density, as illustrated in Figure 2 for selected density fractions from the Dale and WEPSCO DGC separations. Inertinites exhibited the lowest surface area ($15\text{--}25 \text{ m}^2/\text{g}$), isotropic coke particles presented intermediate surface areas ($25\text{--}35 \text{ m}^2/\text{g}$), while anisotropic coke particles exhibited the highest surface areas ($35\text{--}60 \text{ m}^2/\text{g}$). The fly ashes investigated here are class F and were derived from high volatile bituminous coals. Studies on class C fly ashes, that are generally derived from subbituminous coals, have shown much higher surface areas ($200\text{--}400 \text{ m}^2/\text{g}$) [14], indicating that the properties of fly ashes are not only dependent of petrographic composition, but also on the rank of the coal they are derived from. In a previous study, we showed that anisotropic coke, with the greatest BET surface area, appears to adsorb the greatest amount of Hg from the flue gas stream, while inertinite, derived from the coal with little alteration in the combustion process, is the least adsorptive carbon form. Although the relationship between sample density and BET surface area is essentially linear, for Hg adsorption while generally increasing with the density and surface area, does deviate from a simple, linear relationship [15].

Pore size distribution studies were also conducted on the above samples and the proportion of mesopore (pores $2\text{--}50 \text{ nm}$ in width) volume over total volume is presented in Figure 3 for selected density fractions from the Dale separation. Figure 3 shows that for the three carbon types, the pore volume is mainly due to mesopores, with the mesopore volume accounting for over 60% of the total pore volume. This indicates that the extensive and rapid devolatilization that coal undergoes in the combustor, seems to promote the generation of meso- and macropores. There does appear to be a correlation between mesopore volume and carbon type, with inertinites exhibiting the highest proportion of mesopores ($\sim 90\%$), while isotropic coke particles present the lowest fraction of mesopore volume ($\sim 60\%$) and anisotropic coke presenting intermediate values ($70\text{--}80\%$). A similar trend has been found for the WEPSCO DGC fractions.

CONCLUSIONS

Concentrates of three microscopically identifiable forms of unburned carbon (inertinite, isotropic coke, and anisotropic coke) have been generated from two high-carbon-content fly ash samples using the technique of density gradient centrifugation (DGC). The density of like carbon forms isolated from the two fly ashes appears to be quite similar, regardless of the source of the fly ash. The H/C atomic ratios are $\sim 0.028\text{--}0.016$, indicating a high degree of condensation. The surface

areas are relatively low (10-60 m²/g), and most of the pores are in the mesopore range (2-50 nm in width). For both series of fly ash samples, the surface area was found to increase linearly as a function of particle density. This work has shown that the three carbon types are not only visually different, but also present distinctive physical and chemical properties (density, nitrogen and oxygen concentrations, as well as surface area and mesopore volume). Furthermore, these distinctive properties may be reflected in differences in absorption properties, and therefore, the ASTM LOI specification, that is only based on the total carbon content, is not sufficient to identify the suitability of a fly ash for the cement industry. Our immediate goal is to measure the relative capacity of the different carbon types to adsorb air-entrainment reagents. For this purpose, we are developing a micro-technique to measure in-situ the adsorption of such agents directly. Finally, this characterization work has indicated that the unburned carbon can also be considered as a valuable precursor for the production of premium carbon products, since it consists basically of carbon and it has gone through a devolatilization process while in the combustor. Accordingly, we have investigated two potential routes for the generation of premium carbon products from the unburned carbon present in fly ash [16]. The first route focuses on the use of fly ash carbons as precursors for activated carbons by steam activation at 850°C, while the second route concentrates on the utilization of fly ash carbons as a replacement for calcined petroleum coke in the production of carbon artifacts.

ACKNOWLEDGEMENTS

The authors wish to thank Drs. H. Ban and J. M. Stencil (CAER-University of Kentucky) for conducting the triboelectrostatic separation and to the Research Council of the Basque Government for financial support.

LITERATURE CITED

1. The U.S. Department of Energy, 1996, Clean Coal Technology, Reducing emissions of nitrogen oxides via low-NO_x burner technologies, Topic report no. 5.
2. U.S. Environmental Protection Agency, 2000, <http://www.epa.gov/ardpublic>.
3. Hogue, C., 2000, Chemical and Engineering News, **78**, 10.
4. Hower, J.C., Rathbone, R.F., Robl, T.L., Thomas, G.A., Haeblerlin, B.O., and Trimble, A.S., 1997, Waste Management, **17**, 219.
5. Hill, R.L., Sarkar, S.L., Rathbone, R.F. and Hower, J.C., 1997, Cement and Concrete Research, **27**, 193.
6. Freeman, E., Gao, Y-M, Hurt, R.H. and Suuberg, E.M., 1997, Fuel, **8**, 761.
7. Hower, J.C., Rathbone, R.F., Graham, U.M., Groppo, J.G., Brooks, S.M., Robl, T.L. and Medina, S.S., 1995, Proceedings International Coal Testing Conference, 49.
8. Maroto-Valer, M.M., Taulbee, D.N. and Hower, J.C., 1998, Proceedings Conference on Unburned Carbon on Utility Fly Ash, 49.
9. Bailey, J.G., Tate, A., Diessel, C.F.K. and Wall, T.F., 1990, Fuel, **69**, 225.
10. Maroto-Valer, M.M., Taulbee, D.N. and Hower, J.C., 1999, Energy & Fuels, **13**, 947.
11. Taulbee, D.N., Maroto-Valer, M.M. and Hower, J.C., 1999, Proceedings 13th International Symposium on Use and Management of Coal Combustion By-Products, **1**, 24/1-15.
12. Ghosal, S., and Self, S.A., 1995, Fuel, **74**, 522.
13. Palmer, S.R., Sivanandan, S., and Huggett, W., 1997, Proceedings 1997 International Conference on Coal Science, **2**, 1999.
14. Kulatos, I., Gao, Y-M, Hurt, R.H. and Suuberg, E.M., 1998, Prepr. Am. Chem. Soc. Fuel Division, **43**, 980.
15. Hower, J.C., Maroto-Valer, M.M., Taulbee, D.N. and Sakulpitakphon, T., 2000, Energy & Fuels, **14**, 224.
16. Maroto-Valer, M.M., Andr sen, J.M., Andr sen, C.A., Morrison, J.L., and Schobert, H.H., 2000, Prepr. Am. Chem. Soc. Fuel Division, **45**, In Press.

Table 1: Petrographic analysis for the parent samples, carbon-enriched feeds and the highest purity carbon-type density fractions from each separation.

| | Inertinite | Isotropic | Anisotropic | Glass |
|---|------------|-----------|-------------|-------|
| Dale Parent | 3.8 | 13.4 | 19.2 | 63.6 |
| -140 mesh Dale | 1.2 | 2.6 | 5.2 | 91.0 |
| +140 mesh Dale | 2.0 | 13.0 | 25.5 | 59.5 |
| Dale TES (DGC feed) | 5.5 | 24.0 | 61.0 | 9.5 |
| Fraction #2 (1.32-1.65 g cm ⁻³) | 76.5 | 7.0 | 1.0 | 15.5 |
| Fraction #5 (1.72-1.75 g cm ⁻³) | 13.1 | 72.1 | 8.7 | 6.0 |
| Fraction #12 (1.92-1.94 g cm ⁻³) | <0.5 | 19.5 | 76.0 | 4.5 |
| WEPCO parent | 4.0 | 27.3 | 7.3 | 61.5 |
| WEPCO TES (DGC feed) | 8.5 | 51.5 | 27.5 | 12.5 |
| Fraction #4 (1.50-1.60 g cm ⁻³) | 85.5 | 8.5 | 2.5 | 2.0 |
| Fraction #8 (1.725-1.75 g cm ⁻³) | 9.5 | 78.5 | 11.5 | 0.5 |
| Fraction #14 (1.875-1.90 g cm ⁻³) | 2.0 | 20.0 | 75.5 | 2.5 |

Table 2: Elemental analyses of selected density fractions from the Dale carbon-enriched separation.

| Fraction # | Dominant carbon type (vol%) | %C (daf) | %H (daf) | %N (daf) | %O* (daf) | H/C | N/C |
|------------|-----------------------------|----------|----------|----------|-----------|-------|-------|
| DGC feed | 6%in; 24% iso; 61% ani | 97.2 | 0.17 | 1.77 | 0.86 | 0.021 | 0.016 |
| #2 | Inertinite (77 vol%) | 98.4 | 0.21 | 1.44 | < 0.01 | 0.025 | 0.013 |
| #5 | Isotropic (72 vol%) | 95.7 | 0.22 | 1.55 | 2.53 | 0.027 | 0.014 |
| #6 | Isotropic (66 vol%) | 96.5 | 0.13 | 1.55 | 1.82 | 0.016 | 0.014 |
| #10 | Anisotropic (71 vol%) | 97.8 | 0.19 | 1.83 | 0.18 | 0.024 | 0.016 |
| #11 | Anisotropic (71 vol%) | 98.1 | 0.16 | 1.77 | < 0.01 | 0.019 | 0.015 |
| #12 | Anisotropic (76 vol%) | 98.1 | 0.17 | 1.73 | < 0.01 | 0.021 | 0.015 |
| #13 | Anisotropic (73 vol%) | 97.6 | 0.23 | 1.86 | 0.31 | 0.028 | 0.016 |

* Determined by difference

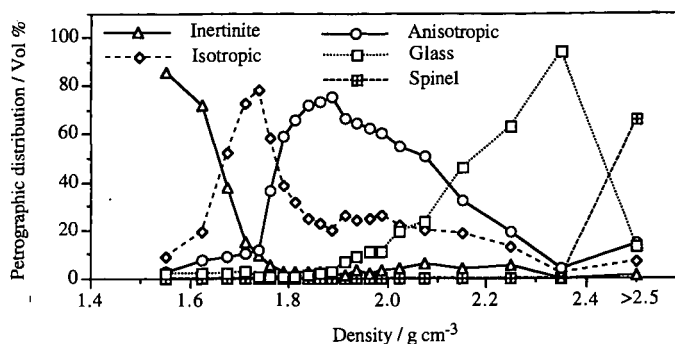


Figure 1: Petrographic distribution of the recovered density fractions for the separation of the WEPCO-TES sample.

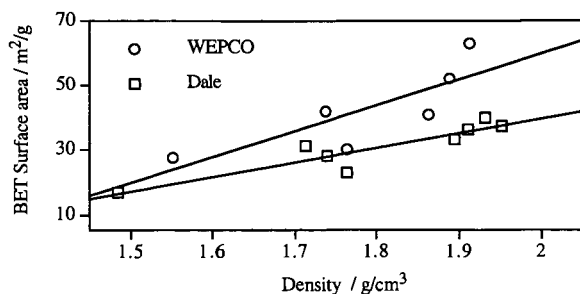


Figure 2: Relationship between surface area and density for selected density fractions from the Dale and WEPCO DGC separations.

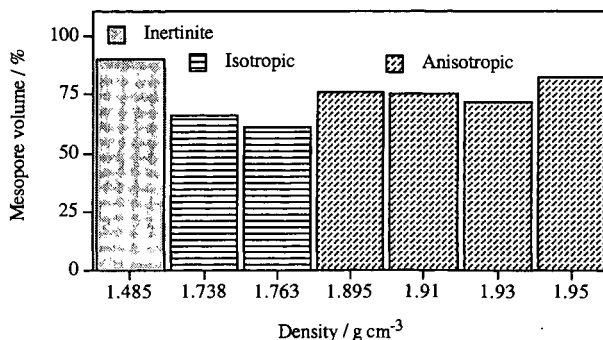


Figure 3: Proportion of mesopore (2-50 nm) volume for selected density fractions from the Dale DGC separation.

TECHNICAL CHALLENGES IN NO_x CONTROL: COST-COMPETITIVE COMPLIANCE FOR COAL-FIRED BOILERS

Stephen A. Johnson and Charles A. Lockert*
ADA Environmental Solutions, LLC
50 Nashua Road, Londonderry NH 03053
*Solvera Particulate Controls

ABSTRACT

In the decade since the Clean Air Act Amendments (CAAA) were enacted, the power generation business has undergone rapid change. In many parts of the U. S., utilities are being restructured into separate generating and distribution companies in preparation for a competitive market for wholesale and retail power. To survive in the emerging marketplace, generating companies are striving to produce the most power (high capacity and availability) for the lowest cost (3 to 3.5 cents per kWh).

At the same time that costs are being reduced, utilities are challenged with meeting tougher new NO_x emission limits imposed by Title IV (acid rain) and Title I (ozone non-attainment) of the CAAA. Title IV limits can generally be met by applying combustion NO_x controls (low-NO_x burners and overfire air) with additional flexibility provided by reburning and selective non-catalytic reduction (SNCR). The cost impacts of these technologies have been recognized and endured. Now Title I will require more drastic NO_x reductions in the 2003 to 2007 timeframe in the 19 eastern states where ozone is highest. The only technology capable of consistently meeting Title I limits is selective catalytic reduction (SCR). Competitive pressures may eventually force all coal-fired plants to meet Title I regulations. The utilities that are able to reduce emissions at the lowest cost will survive.

Since the CAAA were enacted, ADA Environmental Solutions (ADA-ES) has developed and implemented a suite of strategies to reduce the cost of low-NO_x operation through the use of sensors and controls. This paper will provide field data from several plants showing how cost savings were achieved by the test team and maintained by the utility. Examples of cost savings include reduced consumption of SNCR reagent, lower combustion NO_x via biased firing and burners out of service, system-wide NO_x averaging to minimize SCR, reducing the cost of SCR operation by controlling the NO_x going into the reactor, and monitoring and controlling flyash salability by preventing carbon or ammonia contamination.

BACKGROUND

Salem Harbor Station, now owned by PG&E Generating, installed both combustion NO_x controls and Non-selective Catalytic Reduction (SNCR) to meeting NO_x emission goals of 0.33 lb./M Btu for their three coal-fired units. Emission limits were met, but the consumption of urea was a significant operating cost. The original control system metered urea to pre-selected injectors based on a look-up table of inlet NO_x as a function of load generated during pre-retrofit testing by the plant. The urea flow rate was then adjusted to maintain the stack NO_x emission safely below 0.33 lb./M Btu over the load range of each unit. Unfortunately, this control scheme often cranked up the urea flow when furnace temperatures were high, leading to urea combustion instead of NO_x reduction. The author verified the high temperatures by measuring furnace exit gas temperatures (FEGT) with an accurate, on-line, continuous optical temperature monitor called GasTemp. Sootblowing practices had a lot to do with these high temperatures.

RESULTS AND DISCUSSION

First, testing was performed on Units #1 and #2; both 81-MW front-fired boilers equipped with low-NO_x burners and overfire airports. The tests yielded the following conclusions:

- Reagent was injected at the upper end of the temperature window at full load, resulting in only 15 to 22 percent reagent utilization (especially with a dirty furnace at the tail end of a sootblowing sequence).
- Utilization was higher (30-35 percent) at low loads.
- Ammonia slip was experienced, especially during load transients.
- Reagent utilization improved to 26 percent at full load when FEGT was below 2020 F.
- Reagent utilization could be increased to 42 percent at 70% load when FEGT was below 1880 F.

After the initial tests, the plant agreed to modify the control system and incorporate the temperature signal into the control logic for the SNCR system on Unit #3.¹

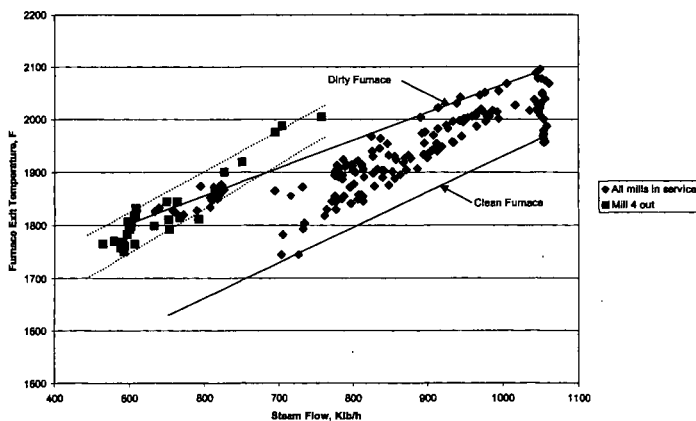
Fuel Tech, the original equipment supplier, designed the control modifications and worked with the plant to install the new software. ADA-ES planned the demonstration tests, collected and analyzed the data, and interpreted the results. The program, results from which are described in reference 1, included 24 days of baseline measurements documenting the original system performance and 35 days of demonstrating the improvements.

Salem Harbor #3 is a front-fired boiler rated at 155 gross MW. The unit is equipped with four levels of urea injectors as well as low-NO_x burners and overfire air to control NO_x emissions below 0.33 lb/M Btu. A complete division wall divides the furnace into two chambers. After the burner retrofit, the unit has had difficulty achieving the designed steam temperature due to lower FEGT. Therefore, furnace sootblowing was only performed a few times a week prior to the test program as necessary to maintain primary superheater steam temperatures below 950 F.

Historical reagent consumption prior to the demonstration varied from 70 to 200 GPH, and averaged about 125 GPH in 1995 and 1996. On the first day of baseline testing, the reagent consumption averaged about 112 GPH over the 24-hour period. On the second test day, operators blew all 36 furnace sootblowers and watched as the reagent consumption at full load dropped to about 62 GPH (the minimum flow allowed by the original control system)! As a result, the operators immediately decided to change their sootblowing practices to better control NO_x. The initial drastic sootblowing decreased reheat steam temperatures by about 15-degrees F, but also reduced superheater attenuator spray flows from 52,000 to 15,000 lb/h. Reheat steam temperatures recovered in a matter of hours, but the reagent consumption continued at the minimum level for another day. Further experience indicated that frequent sootblowing using only a few blowers at a time could maintain low reagent consumption without any adverse effects on boiler performance.

FEGT at full load varied from 1950 to 2100 F, depending on sootblowing, as shown on Figure 1. As a result of this "baseline" testing experience, the FEGT signal was incorporated into the revised control system.

Fig. 1 Relationship of FEGT to Steam Flow at Salem Harbor #3



The changes to the SNCR system included mechanical upgrades, new instrumentation, and software replacement. Fuel Tech first installed a remote pressure regulator on each reagent metering module so that atomizing pressure and reagent flow could be controlled across the load range at each injection elevation. This modification allowed flexibility to use temperature to dictate system operation. Then Fuel Tech updated the Allen-Bradley and FactoryLink software to include the temperature signal among other changes listed in Table 1.

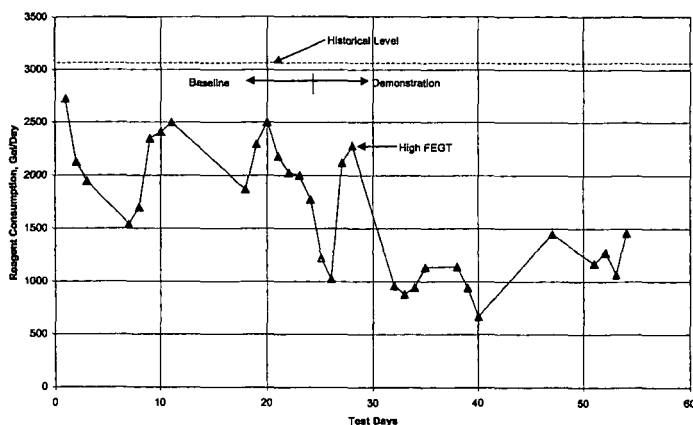
The results achieved with the new control system were dramatic. Figure 2 shows daily reagent consumption for both the baseline and demonstration periods. Historical reagent usage had been over 3000 gal/day based on Unit #3's share of the total station consumption. During the baseline test period, consumption ranged from 1500 to 2700 gal/day, depending on how the operators

chose to apply the IR sootblowers. Sootblowing schedules were formally introduced in order to maintain FEGT at full load in the range of 1950 to 2000 degrees F during the demonstration period in conjunction with the control system modifications. As a result, the reagent consumption was reduced to 600-1500 gal/day (less than half of the historical level). Moreover, these savings were sustainable after the test crew had gone home. The resulting cost savings was estimated by the plant to be about \$600K/y at a urea price of \$0.90/gallon.

Table 1. Software Changes

| Original Control System | Upgraded Control System |
|---|---|
| Initial reagent flow rate selected from look-up tables based on steam flow and mills in service. | Initial reagent flow rate calculated from curves based on steam flow and FEGT. |
| Look-up table values for reagent flow were established during tests when sootblowers were not used. | The reagent flow curves extended to much lower values based on the sootblower performance data. |
| Injector liquid pressure constant. | Injector pressure varied with rate of temperature change. Rapid FEGT decrease results in reduced atomizer pressure, thus reducing both reagent flow rate and droplet size. |
| NO _x set point selected automatically, but operator override possible. | Included a new screen showing average daily NO _x and projected NO _x if current set point is maintain. Operators could then adjust set point to reduce reagent flow at the end of the day and still assure compliance. |
| System response time set to avoid instabilities given original inputs. | System response time shortened to take advantage of new inputs. |

Figure 2. Daily Reagent Use at Salem Harbor #3



Biased Firing and BOOS: a Poor Man's OFA.

Another low-cost step for reducing NO_x from existing boilers is to increase the amount of staged combustion that the boiler can achieve. Figure 3 shows a general relationship between NO_x emissions and stoichiometric ratio at the lower burners. The background data for this curve are somewhat complicated to explain^{2,3,4}, but the main points are that NO_x can be further reduced when:

1. The SR approaches 0.7
2. The OFA ports are located well above the top burner elevation.

The poor-man's way to achieve these low-NO_x conditions is to try biased firing and burners out of service. Biased firing increases the size of locally fuel-rich regions within the flame zone by

redistributing the air and fuel within the furnace. To best reduce NO_x , the fuel should be biased lower or toward the middle of the furnace, while the air is biased upward and toward the furnace sidewalls. The result is to decrease the SR for the lower (or center) burners, and increase the SR for the upper (or wing) burners and OFA ports. Since NO_x emissions decrease more drastically at low SR than they increase at high SR, the overall result is usually a substantial NO reduction. The only trick is choosing fuel-rich burners such that their flames will contact enough combustion air in the upper furnace to complete burnout.

Biased firing taken to the extreme is taking burners out of service entirely. In this case, the lower burners are operated fuel-rich, while the upper burners are operated on air only and essentially become a second set of OFA ports. Flame-zone NO_x reduction is maximized at a SR of 0.7, the additional residence time between active burners and OFA ports enhances NO_x reduction, and very little NO_x is formed in the burnout zone as long as burnout is slow.

To take advantage of BF/BOOS, the operator must have accurate control over fuel and airflow to each burner. On-line measurement of both air and fuel can be achieved by installing flow sensors in the burner lines. Alternatively, combustion optimization software has been used to help operators maintain BF/BOOS conditions. The software will often select biased firing conditions from the normal operating range as lowest possible NO_x . Given total airflow to the burners and overfire air ports, the software can learn to control biased firing, even if fuel distributions are not well characterized. If the fuel flow to each burner is measured, the system is even more robust.

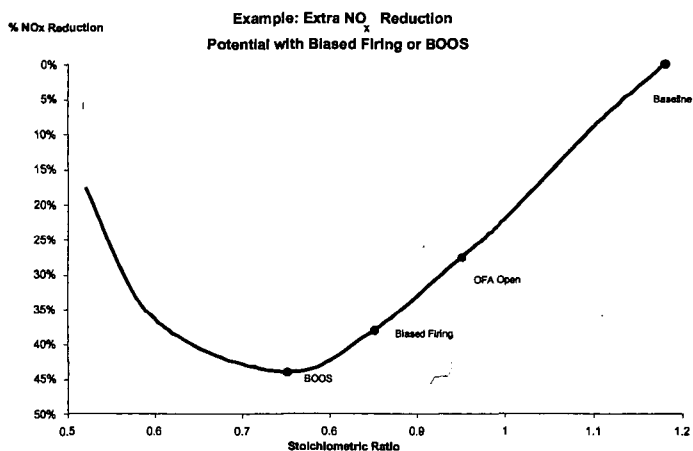
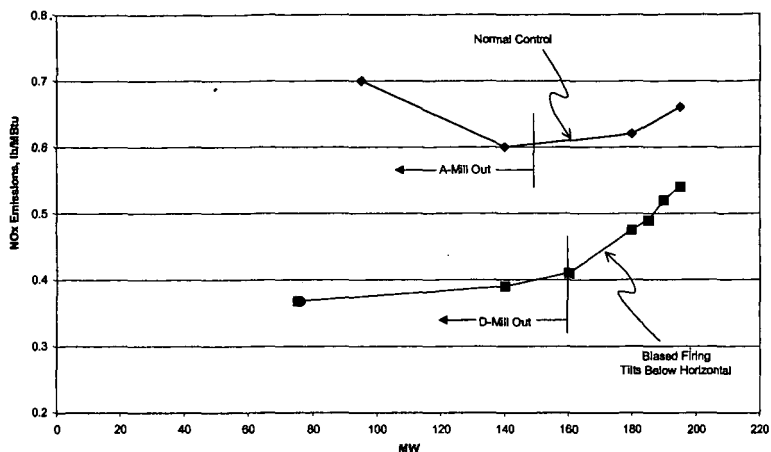


Figure 3. NO_x Reduction from Staged Combustion.

ADA-ES has recently completed a test series on a 180-MW tangentially fired boiler already equipped with closed-coupled OFA ports. Figure 4 shows the trends of NO_x with load before and during the tests. The situation at this utility is that they need to meet Title IV NO_x limits now while looking ahead to Title I. Low-cost NO_x control will partially offset the cost of credits in the nearterm, and reduce the cost of SCR (if required) in the long term. It can be seen that BF/BOOS can achieve up to 50% reduction in low-load NO_x , and 20% NO_x reductions are sustainable at full load. BF/BOOS operation has been adopted by the operators and is now the preferred mode of operation.

Figure 4.
NO_x Emissions Vs. Load at a 180 MW Tangential Unit



System-Wide NO_x Averaging.

Title I NO_x controls will be enforced within each state on a system-wide basis. Therefore, another way to save money on NO_x control is to over-control NO_x on units that have advantages and under-control NO_x on other units where there are barriers to NO_x control. Since SCR is the most expensive control method in terms of \$/ton of NO_x removed, the objective of this strategy is to juggle the suite of NO_x-control technologies such that the fewest number of SCR units are required.

One utility company that we have worked with operates 24 boilers in two states. Since most of these boilers already used low-NO_x burners and overfire air for NO_x control, they only needed 10 SCR units on their largest boilers to achieve a system-wide average NO_x of 0.15 lb/M Btu. Accordingly, high performance SCR treats flue gas from equipment that generates 72% of the seasonal power production. However, this was not the least-cost scenario.

To reduce compliance costs, ADA-ES walked down each unit and examined design and operating data to determine additional NO_x reduction potential. Technologies considered included:

- Biased firing/burners-out-of-service
- Low-NO_x burners (if not already there)
- Overfire air booster fan for deeper staging
- Optimization software and sensors for temperature, LOI, per-burner coal flow
- Conversion to natural gas
- Reburning with coal or natural gas
- Fuel lean gas reburning
- Amine-enhanced gas reburning
- Selective non-catalytic reduction

Several units in this system have spare mill capacity and sufficient furnace volume to take maximum advantage of BF/BOOS. Therefore, it was not surprising that some combination of BF/BOOS, optimization software, and SNCR for the smaller megawatt units saved considerable money. In addition, by applying these techniques in all 24 boilers, the NO_x emission limit could be met using only seven SCR units. The overall savings were about \$17M/y.

SCR Control Improvements.

There are now ten Selective Catalytic Reduction (SCR) NO_x control systems operating in the United States on coal-fired boilers. Within the next year, SCR technology will be adopted by many other utilities faced with meeting low NO_x emission limits driven by Title I of the Clean Air Act Amendments. Currently, there are an estimated 40 SCR units either under construction or in procurement within the Ozone Transport Region. Estimates of the number of SCR units to be built between now and 2007 in the US range from 80 to 200.

SCR systems employ relatively simple instrument and control (I&C) schemes to meter the correct amount of ammonia into the flue gas to maintain NO_x below the regulated value. System designs contain some margin of safety to account for the range of temperature, inlet NO_x concentration, or particulate matter expected under steady-state conditions. However, these parameters can change very quickly during transient operation (load swings, start-up, shutdown) or off-design operation (mills or burners out of service, feedwater heaters out of service). Also, the local NO_x or temperature distributions can change at the ammonia injection point, even though the total NO_x or heat input remains the same. The results could be wasted reagent or worse, the formation of ammonium sulfate or bisulfate that can foul air preheater surfaces, contaminate flyash that the utility may want to sell, and increase stack opacity above regulated limits.

Weaknesses in conventional SCR control systems, as described by operators, include:

- Unreliable NO_x analyzer sampling system upstream of the SCR reactor.
- Slow ammonia reagent flow response based on a 5 to 10 minute lag time in the feedback NO_x signal from the stack CEM.
- Over-feeding ammonia reagent when the SCR inlet NO_x concentration undergoes a step change decrease (as occurs when a top mill is taken out of service or a lower mill is put into service).
- Reagent flow reverts to default values during CEM calibration.

ADA Environmental Solutions, LLC (ADA-ES) was contracted by EPRI to evaluate SCR design and operating data from US SCR installations in order to quantify the extent of any adverse impacts from the problems listed above. We then evaluated whether improvements can be made to existing control systems to manage potential side effects of SCR, which could include air heater fouling, flyash contamination, catalyst poisoning, or stack opacity.

Control system upgrades devised by ADA-ES were described in two papers given at the recent EPRI/EPA/DOE Mega Symposium ^{5,6}. However, one of the most effective ways to reduce the cost and risk of SCR operation is to minimize the NO_x concentration going into the reactor. Lower inlet NO_x means lower ammonia consumption and lower ammonia/ NO_x ratios. The ammonia/ NO_x ratio defines the risk of ammonia slip: if the ratio can be held less than 0.8, then the ammonia slip will not exceed 1 PPM. The catalyst lifetime (defined as the time until ammonia slip exceeds 2 PPM) can also be increased significantly when the inlet NO_x is low. Biased firing was one technique recommended by ADA-ES to reduce ammonia/ NO_x ratio.

Recent operating experience at Stanton has incorporated many of the improvements suggested by the results of this EPRI project. In their third year of operation, Stanton experienced higher than expected catalyst deactivation, which motivated operators to modify combustion to reduce NO_x going into the SCR. One change that worked well was operating with the top mill (out of five) out of service to increase the staging effect. This allowed Stanton to reduce boiler outlet NO_x from 0.4 to as low as 0.26 lb./M Btu, and consistently maintain this value below 0.32 lb./M Btu! Another change was to move the NO_x emission set point closer to the permitted NO_x value. As a result of these improvements, reagent consumption has dropped to about 200 lb./h at full load, saving about 25%, and ammonia slip episodes have been less frequent. Further efforts are underway to improve the feedback NO_x signal from the stack CEM to achieve faster response to load swings.

Improved Flyash Sales

Before the CAAA, utilities found it easy to meet unburned carbon specifications for flyash sold to use in cement and concrete products. Flyash loss-on-ignition (LOI) must be below 3-5% in order to prevent absorption of air entrainment chemicals used in the cement industry to control the strength and prevent cracking of concrete products. Flyash sales also represent a significant revenue stream for some utilities. The difference between landfill costs and flyash sales can be as much as \$25/T. A 500 MW coal-fired unit firing a bituminous coal will produce about 280 tons/day of flyash, which could represent about \$2M/y in revenues and avoided costs.

ADA-ES has been working with Solvera Particulate Controls, Inc to help utilities realize these cost benefits. Solvera has obtained the rights to the CAMRAC online LOI monitor⁷, and has applied this monitor to determine whether flyash removed from the precipitator is saleable or not. In this application, the LOI monitor takes an ash sample from the pneumatic line under each collection hopper. Solvera has also mounted the LOI monitor in the economizer outlet duct and

developed reliable procedures to extract a representative, isokinetic sample for analysis every ten minutes. The resulting LOI readings are accurate and close enough to real time to make online combustion tuning feasible.

ADA-ES has recently installed the CAMRAC on a 50 MW coal-fired boiler to measure and reduce LOI that impairs precipitator performance. First, the instrument will be used to troubleshoot the root cause of the LOI problem. The problem developed after installation of low- NO_x burners, but changes to burner operation (airflow distribution, primary airflow) or sealing windbox leaks into the furnace may help alleviate the problem. We will also try biased firing for simultaneous NO_x and LOI reduction. We have already talked about the NO_x benefits of BF/BOOS. Sometimes this technique can also reduce LOI by injecting more coal lower into the furnace, thus extending combustion burnout time for more of the fuel. As of this writing, no data are available from this test but results should be ready to incorporate into the presentation of this paper in August.

CONCLUSIONS

Meeting the NO_x emission limits required by Title IV and Title I of the CAAA can be costly, but cost improvements are possible for most boiler operators. The key to achieving cost savings is to monitor and control those factors that can be related to cost. For SNCR installations, the furnace temperature at the point of reagent injection can be monitored and controlled to maximize reagent utilization. In the example given above, utilization was doubled from less than 20 percent to over 40 percent. For SCR, it is cost-effective to monitor and minimize the NO_x concentration coming into the reactor to save on reagent cost. For both these technologies, reducing NH_3/NO_x ratios will also cut back on ammonia carryover, a major cause of air heater pluggage and possible source of flyash contamination.

Combustion NO_x controls (low- NO_x burners, overfire air, reburning) slow down the combustion process, often leading to more unburned carbon in the flyash unless operators can make adjustments. Combustion NO_x controls also decrease the margin of error for maintaining per-burner air-fuel ratios, since a single burner can produce enough carbon to contaminate the flyash product. Sensors are available to monitor LOI and furnace temperature. LOI provides direct feedback for combustion tuning and other firing strategies to reduce NO_x . It is also a required input for optimization software systems that provide operators with operating settings for maintaining NO_x within compliance while not exceeding LOI or heat rate constraints. Furnace temperature can also be used by these optimization systems as a way to measure and control boiler heat balance.

Payback for sensor-driven systems can be very rapid. The reward is reliable emission compliance and more power sales in a competitive market.

REFERENCES

1. R Afonso, A Sload, D Miles, S Johnson, and J O'Leary, "Enhanced NO_x OUT Control at Salem Harbor Unit #3, presented at the EPRI-DOE-EPA Mega Symposium, Washington, DC, August 1997.
2. Johnson, S. A., "NO_x Control by Burner and Furnace Design," Chapter in Energy Technology Handbook edited by Douglas Considine, McGraw-Hill Publishers, NY, NY 1978.
3. Johnson, S. A. and Sommer, T. S., "Commercial Evaluation of a Low- NO_x Combustion System as Applied to Coal-Fired Utility Boilers," Proceedings of the Joint Symposium on Stationary Combustion NO_x Control, Volume 1, EPRI Report WS-79-220, Palo Alto, CA, May 1981.
4. Lisauskas, R. A., Snodgrass, R. J., Johnson, S. A., and Eskanazi, D., "Experimental Investigation of Retrofit Low- NO_x Combustion Systems," Presented at the 1985 Joint Symposium on Stationary Combustion NO_x Control, May 1985.
5. Johnson, S. A., Zammit, K. D., and Engelmeyer, A. J., "Improved SCR Control to Reduce Ammonia Slip", presented at the EPRI-DOE-EPA Mega Symposium, Atlanta, GA, (EPRI Report TR-113187-V2) August 1999.
6. Comer, J. P. and Johnson, S. A., "SCR Sootsniffers: a New NO_x Process-Monitoring Tool", presented at the EPRI-DOE-EPA Mega Symposium, Atlanta, GA, (EPRI Report TR-113187-V2) August 1999.
7. DiGioia, A. and Trelice, D., "In-Duct Monitoring of Flyash LOI for Ash Quality and NO_x Control" presented at the Southeastern Electric Exchange, November 1996.

A NEW PATH TO "PROMPT" NO: CH + N₂ = H + NCN STUDIED BY AB INITIO MO AND STATISTICAL THEORY CALCULATIONS

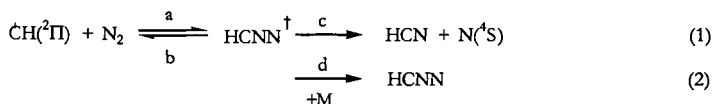
M. C. Lin, L. V. Moskaleva, And Wensheng Xia
Department of Chemistry
Emory University, Atlanta, GA 30322, USA

ABSTRACT

In the past two decades, the CH(²Π) + N₂ → HCN + N(⁴S) reaction has been routinely employed for kinetic modeling of NO_x formation in hydrocarbon combustion. The reaction has been studied by many investigators¹⁻¹⁷ since Fenimore¹⁸ suggested it to be a potential "prompt" NO precursor process in 1971. The result of a recent comprehensive study by Morokuma and co-workers,^{19,20} however, indicated that the theoretically predicted rate constant for the formation of the spin-forbidden HCN + N products is about two orders of magnitude lower than experimentally measured values.^{1,2,7,8} The result of our high-level molecular orbital study aided by a statistical-theory calculation reveals that the spin-allowed H + NCN products occurring by the ground electronic doublet surface is the dominant CH + N₂ process under combustion conditions.

INTRODUCTION

The kinetics of the reaction available prior to 1983 were first interpreted in terms of the global mechanism involving an internally excited HCNN adduct:



by Berman and Lin,⁴ who measured the pressure-dependent bimolecular rate constant (*k*₂) by laser-induced fluorescence, monitoring the decay of CH at temperatures between 297 and 675 K. Their low-temperature, pressure-dependent data, which have been corroborated in subsequent independent studies,^{9,10} were correlated with high-temperature NO formation results by Blauwens et al.¹ with the Rice-Ramsperger-Kassel-Marcus (RRKM) theory. More recently, there have been two shock-tube studies at high temperatures, monitoring either CH decay by laser absorption spectroscopy or N production by atomic resonance absorption spectroscopy, providing the much needed high-temperature kinetic data.^{7,8}

Theoretically, the production of N atoms by reaction (1) has been investigated by Manna and Yarkony^{13,14} on the nature of the doublet-quartet curve crossing and by Walch¹⁵ and Seideman and Walch¹⁶ on the potential energy surface (PES) involved. Miller and Walch¹⁷ recently calculated *k*₁, ignoring the retarding effect of the doublet-quartet crossing, with the RRKM theory above 1000 K and concluded that the high-temperature shock-tube data of Hanson, Roth and co-workers^{7,8} can be satisfactorily accounted for. On the other hand, the result of a more comprehensive calculation by Morokuma and co-workers²⁰, based on a more detailed PES¹⁹ with the inclusion of the curve crossing effect, indicated a rather poor agreement between theory and experiment as alluded to above.

RESULTS AND DISCUSSION

In this work, we study the mechanism of the CH + N₂ reaction, centering on the reaction path over the ground electronic doublet PES. The result of this high-level *ab initio* molecular orbital calculation, aided by a multichannel RRKM analysis and kinetic modeling for CH decay and N production reveals unambiguously that the prompt NO observed in hydrocarbon flames actually arises primarily from the spin-allowed reaction,



The reaction occurs via two NC(H)N ring intermediates and the HNCN radical. The prompt NO can be formed by the facile, exothermic oxidation of NCN by O, OH and O₂ present in the flame.

The PES of the ground electronic doublet state, shown in Fig. 1 with a relevant portion of the quartet state leading to HCN + N, has been computed with the G2M method.²¹ The method employed is the same as previously used by Cui and Morokuma.¹⁹ The geometries were

optimized at the B3LYP level (Becke's three parameter density functional²² with the nonlocal correlation functional of Lee, Yang, and Parr²³) with the standard 6-311G(d,p) basis set. The vibrational frequencies used for characterization of stationary points, ZPE corrections and RRKM calculations, were computed at the same level of theory. All MO calculations were performed with the Gaussian 94²⁴ and MOLPRO96²⁵ program packages.

The quartet portion of the potential energy surface is entirely taken from ref. 19. On the doublet surface we found a concerted path connecting a ring intermediate, INT2, with the HNCN radical, the latter can dissociate to H + NCN. The endothermicity of this channel is 21.5 kcal/mol at the G2M level, while the concerted transition state, TS3, is 11.7 kcal/mol above the reactants at the same level of theory. The connections of this transition state to respective minima on the PES were established by an IRC test.²⁶

Since for the last part of the potential energy surface (HNCN dissociation) no distinct transition state could be found, we mapped out a one dimensional dissociation profile at the B3LYP level and fitted it with Morse potential, adjusting D_e to the respective G2M value afterwards. The resulting potential can be effectively represented by the equation, $V(r) = D_e(1 - e^{-\beta(r-r_0)})^2$, where $D_e = 84.01$ kcal/mol, $\beta = 3.27$, $r_0 = 1.160$ Å. A canonical variational RRKM calculation was performed based on the G2M energies and calculated B3LYP molecular parameters at each point along the dissociation curve for $\text{HNCN} \rightarrow \text{H} + \text{NCN}$.

Although the doublet product channel, $\text{NCN} + \text{H}$, is 18.1 kcal/mol higher than $\text{HCN} + \text{N}$, it is 0.8 kcal/mole lower than the last barrier leading to the formation of the latter products on the quartet surface. The apparent barrier for the HNCN dissociation would be much lower at high temperatures because of the entropic contribution, which reduces the values of ΔG^\ddagger as the temperature increases. The theoretically predicted heat of formation for the NCN radical at 0 K based on reaction (3), 111.0 kcal/mol, is in good agreement with the recently reported experimental values: by Neumark and co-workers²⁷, 111.3 kcal/mol, and by Clifford et al.²⁸, 107.4 ± 3.2 kcal/mol.

The rate constant for the production of NCN by reaction (3) was calculated with a multichannel RRKM program previously used in our study of the $\text{NH}_2 + \text{NO}$ reaction.²⁹ The result of the calculation compares closely with those measured at high temperatures purportedly for k_1 , based on either the decay of CH^6 or the formation of N^7 . In the temperature range, 1500-4000 K, the predicted k_3 at 0.88 atm can be represented by the modified Arrhenius expression, $k_3 = 2.22 \times 10^7 T^{4.48} \exp(-11760/T)$ $\text{cm}^3/(\text{mol}\cdot\text{s})$.

SUMMARY AND CONCLUSIONS

To conclude, we have demonstrated that the $\text{CH} + \text{N}_2 \rightarrow \text{H} + \text{NCN}$ reaction, which occurs over the ground electronic doublet PES, is spin-allowed and more favorable than the accepted, spin-forbidden path producing $\text{HCN} + \text{N}$. The computed rate constant for CH decay agrees quantitatively with experimentally measured values.⁸ In addition, the predicted N-atom production rate also agrees fully with experimental result⁷ within the scatter of typical shock-tube data. Under combustion conditions, NO can be formed readily by the rapid oxidation of NCN by O, OH and O₂.

ACKNOWLEDGEMENTS

LVM thanks the Division of Chemical Science, U.S. Department of Energy, for the support. WX and MCL acknowledge the support from the Caltech MURI project through the Office of Naval Research.

REFERENCES

1. Blauwens, J., Smets, B. & Peeters, J. *Combust. Inst.* **16**, 1055-62 (1977).
2. Matsui, Y. & Nomaguchi, T. *Combust. Flame*, **32**, 205-14 (1978).
3. Butler, J. E., Goss L. P., Lin, M. C. & Hudgens, J. W. *Chem. Phys. Lett.* **63**, 104-7 (1979).
4. Berman, M. R., Lin, M. C. *J. Phys. Chem.* **87**, 3933-42 (1983).
5. Duncanson, J. A., Jr., Guillery, W. A. *J. Chem. Phys.* **78**, 4958-62 (1983).
6. Matsui, Y. & Yuuki, A. *Jpn. J. Appl. Phys.* **24**, 598-603 (1985).
7. Lindackers, D., Burmeister, M., Roth, P. *Combust. Inst.* **23**, 251-57 (1991).
8. Dean, A. J., Hanson, R. K. & Bowman, C. T. *Combust. Inst.* **23**, 259-65 (1991).

9. Becker, K. H., Engelhardt, B., Geiger, H., Kurtenbach, R., Schrey, G. & Weisen, P. *Chem. Phys. Lett.* **195**, 322-328 (1992).
10. Medhurst, L. J., Garland, N. L. & Nelson, H. H. *J. Phys. Chem.*, **97**, 12275 (1993).
11. Morley, C. *Combust. Flame*, **27**, 189-204 (1976).
12. Miller, J. A., Bowman, C. T. *Prog. Energy Combust. Sci.*, **15**, 287-338 (1989).
13. Manna, M. R. & Yarkony D. R. *J. Chem. Phys.* **95**, 1808-1816 (1991).
14. Manna, M. R. & Yarkony D. R. *Chem. Phys. Lett.* **188**, 352-358 (1991).
15. Walch, S. P. *Chem. Phys. Lett.* **208**, 214-18 (1993).
16. Seideman, T. & Walch, S. P. *J. Chem. Phys.* **101**, 3656-61 (1994).
17. Miller, J. A., Walch, S. P. *Int. J. Chem. Kinet.* **29**, 253-259 (1996).
18. Fenimore, C. P. *Proc. Combust. Inst.* **13**, 373-79 (1971).
19. Cui, Q., Morokuma, K. *Theor. Chem. Acc.* **102**, 127-133 (1999).
20. Cui, Q., Morokuma, K., Bowman, J. M., and Klippenstein, S. *J. Chem. Phys.* **110**, 9469-82 (1999).
21. Mebel, A. M., Morokuma, K. & Lin, M. C. *J. Chem. Phys.* **103**, 7414-21 (1995).
22. Becke, A. D. *J. Chem. Phys.* **98**, 5648-52 (1993).
23. Lee, C., Yang, W. & Parr, R. G. *Phys. Rev. B*, **37**, 785-9 (1998).
24. M. J. Frisch, G. W. Trucks, H. B. Schlegel, P. M. W. Gill, B. G. Johnson, M. A. Robb, J. R. Cheeseman, T. Keith, G. A. Petersson, J. A. Montgomery, K. Raghavachari, M. A. Al-Laham, V. G. Zakrzewski, J. V. Ortiz, J. B. Foresman, J. Cioslowski, B. B. Stefanov, A. Nanayakkara, M. Challacombe, C. Y. Peng, P. Y. Ayala, W. Chen, M. W. Wong, J. L. Andres, E. S. Replogle, R. Gomperts, R. L. Martin, D. J. Fox, J. S. Binkley, D. J. Defrees, J. Baker, J. P. Stewart, M. Head-Gordon, C. Gonzalez and J. A. Pople, *GAUSSIAN 94, REVISION A.1*; Gaussian, Inc., Pittsburgh PA, 1995.
25. MOLPRO is a package of *ab initio* programs written by H.-J. Werner and P. J. Knowles, with contributions from J. Almlöf, R. D. Amos, A. Berning, D. L. Cooper, M. J. O. Deegan, A. J. Dobbyn, F. Eckert, S. T. Elbert, C. Hampel, R. Lindh, A. W. Lloyd, W. Meyer, A. Nicklass, K. Peterson, R. Pitzer, A. J. Stone, P. R. Taylor, M. E. Mura, P. Pulay, M. Schütz, H. Stoll and T. Thorsteinsson.
26. Gonzalez, C. Sosa, C., and Schlegel, H. B. *J. Phys. Chem.* **93**, 2435-40 (1989).
27. Bise, R. T., Choi, H., Neumark, D. H. *J. Chem. Phys.* **111**, 4923-32 (1999).
28. Clifford, E. P., Wentholt, P. G., Lineberger, W. C., Petersson, G., and Ellison, G. B. *J. Phys. Chem.* **101**, 4338-45 (1997).
29. Diau, E. W., Wagner, M. A. G. & Lin, M. C. *J. Phys. Chem.* **98**, 4034-42 (1994).

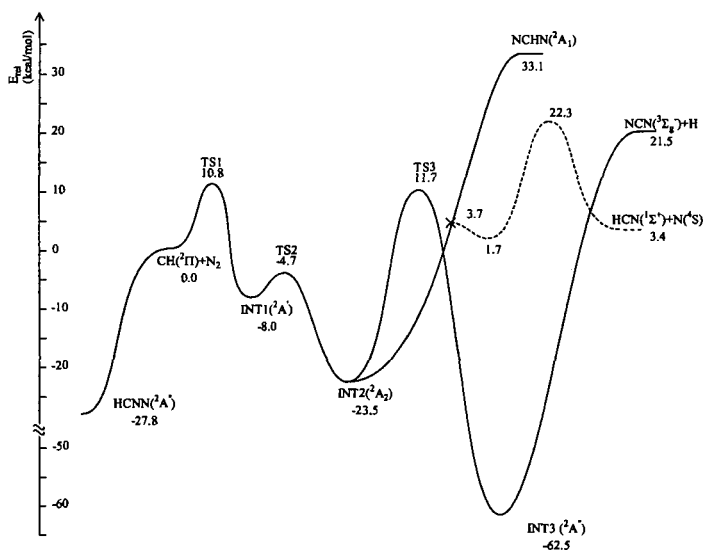


Figure 1. Potential energy diagram for reaction (3) combining the result of Cui and Morokuma¹⁹ for the quartet state given by the dotted curve where "x" indicates curve crossing with the present work for the doublet state given by the solid curve. The relative energies are calculated at the G2M(RCC) level including B3LYP/6-311g(d,p) ZPE correction.

PREDICTING AROMATICS FORMATION FROM PROPARGYL REACTIONS: DEVELOPMENTS IN AROMATICS-FORMATION MODELING IN THE 1990'S

Phillip R. Westmoreland* and George E. Oulundsén
Department of Chemical Engineering; University of Massachusetts Amherst
Amherst, MA 01003-3110; westm@ecs.umass.edu

KEYWORDS: propargyl, soot, combustion, chemical activation, benzene, phenyl

ABSTRACT

Predicting the formation of aromatics and soot is a long-sought goal for combustion design, and propargyl (C_3H_3) chemistry appears to be a key. Self-combination reactions and addition to propyne or propadiene have all been proposed to form aromatic rings. Some of these proposals have been based on careful calculations or on clean experimental data. However, the picture is quite complex and in dispute because of the complex rearrangements that can result from chemical activation. Using theory and experiment, I will discuss the controversy over the various proposed kinetics. In the next ten years, we should be able to establish the correct kinetics and use it for engineering analysis and design.

INTRODUCTION

Clean air was one of the central concerns as the environmental movement grew though the 1960's, and sooty air has been one of the worst offenders throughout time. Percival Pott's recognized in the 18th century that combustion-generated soot was linked to cancer, but this insight only led to better personal hygiene requirements for chimney sweeps, not to reduced amounts of soot. Indeed, coal use in the 19th century's Industrial Revolution exacerbated the problem. Reduction began in the 20th century, spurred by an increased scale of industry and increased acceptance of individual rights relative to those industries, and aided by the use of natural gas and new environmental control technologies. A US landmark was the 1970 formation of the Environmental Protection Agency.

Twenty years later, the Clean Air Act of 1990 pushed industry to reduce emissions of smog-forming chemicals, carbon monoxide, and particulates up to $10\text{ }\mu\text{m}$ in size, such as soot. Incentives were mixed with regulation. Subsequent 1997 amendments led to tightening by adding specific standards for particulate matter smaller than $2.5\text{ }\mu\text{m}$.

The US Department of Energy, Department of Defense, and Environmental Protection Agency, as well as government agencies around the world, have long supported research to identify the chemical pathways that form soot. The guiding hypothesis is that by knowing the pathway, it can be interfered with to prevent or destroy soot. Wagner's 1980 review [1] concluded that soot was made of small graphitic domains of polycyclic aromatic hydrocarbons (variously acronyms as PAH, PCA, or PNA). A large body of work, most notably the daring model of Frenklach *et al.* in 1984 [2], pointed to formation of the first aromatic ring as being the rate-determining step for growth toward soot.

Propargyl (linear C_3H_3 , $CHCCH_2$) has gained wide support as the key precursor to aromatic hydrocarbons in flames, but its dominance, reaction pathway(s), and kinetics are still controversial. This paper examines the competing ideas in the context of recent calculations and data.

BACKGROUND: LITERATURE ON AROMATICS FORMATION

In 1989, Westmoreland *et al.* [3] reviewed the precursors and routes to single-ring aromatics which had been proposed to date. Previous mechanistic proposals had focused on molecular pathways (polyacetylene bridging, Diels-Alder additions), ion-molecule reactions, and radical addition or combination. Modeling their acetylene flame data [3] showed that only the radical routes:

- $n\text{-C}_4\text{H}_5 + \text{C}_2\text{H}_2$ (-CHCHCHCH_2 , route proposed by Cole *et al.* [4]);
- $n\text{-C}_4\text{H}_3 + \text{C}_2\text{H}_2$ (-CHCHCCH , proposed by Stehling *et al.* [5] and by Frenklach *et al.* [2]), and/or
- $\text{C}_3\text{H}_3 + \text{C}_3\text{H}_3$ (proposed in the literature by Kern and co-workers [6-7])

could be fast enough, necessarily proceeding by chemically activated isomerizations rather than thermal steps. However, they could not establish which of the three reactant pairs dominated, nor whether the detected C_4H_5 and C_4H_3 were the proper isomers.

Several possible propargyl paths then were proposed around the early 1990's:

- In 1989, we subsequently proposed [8] and later tested [9] a chemically activated pathway from C_3H_3 via chemically activated 1,5-hexadiyne and 1,2,4,5-hexatetraene, isomerizing to 3,4-dimethylenecyclobutene (DMCB). Corresponding thermal isomerizations are recognizable as a Cope rearrangement and a 2+2 sigmatropic ring closure. We proposed that DMCB might isomerize to fulvene (methylenecyclopentadiene) and then to benzene, possibly decomposing to phenyl + H. Chemical activation at the low-pressure (adiabatic) limit could allow reaction above all these intrinsic barriers. Reaching any well would require bimolecular collisions. This hypothesized route was based on thermal pyrolyses of the intermediates. Our reaction modeling [9] implied that phenyl would be an important product at high temperatures.
- Stein and co-workers [10] developed a similar route independently and at about the same time, using their VLPP data and the flame data of Ref. [1]. It proposed that DMCB might isomerize directly either to fulvene or benzene.
- Alkemade and Homann proposed another route [11] involving cyclopropenyl intermediates.
- Miller *et al.* [12] had proposed formation of benzene from propargyl, and Melius, Miller, and Evleth [13] later proposed a variety of routes based on singlet carbene intermediates, BAC-MP4/MP4/6-31G(d,p)/UHF/6-31G(d) potential energy surfaces, and adiabatic RRKM calculations. The end products were phenyl + H.

These promising proposals do not mean that we know that aromatics are formed from propargyl or that we know by what rate. Modeling by Frenklach *et al.* [14] in 1997 implied that the C_4H_3 route might be more important than the C_3H_3 route in some flames and at lower temperatures. Likewise, $C_3H_3+C_3H_4$ is still discussed, and $C_3H_3+C_3H_5$ routes have been proposed and supported by using assumed rate constants in large-mechanism modeling of shock-tube and flame data [15]. Finally, the different possible channels from $C_3H_3+C_3H_3$ will have different pressure dependences. In lieu of clean, direct measurement of rates and products at high temperatures, we must make use of more complex flame data and of calculations.

EXAMINING FLAME DATA

Recent MBMS measurements in an allene-doped ethylene flame by Oulundsen [16] allow comparisons to species in a matching undoped flame of Bhargava and Westmoreland [17]. Although most species are unperturbed, C_3 's and C_6H_6 are affected.

Molecular-beam mass spectrometry (MBMS) was used to measure profiles of free-radical and stable-species mole fractions in one-dimensional flames (Table 1). Both flames had the same fuel-rich equivalence ratio $\phi = 1.90$ (fuel-rich), pressure of 2.666 kPa (20.00 Torr), and velocity at the burner of $u_{b-300} = 62.5$ cm/s. The doped flame was composed of 0.50 % allene, C_2H_4 , O_2 , and 49.7 % Ar, in comparison to the undoped flame with only C_2H_4 , O_2 , and 50.0 % Ar. The profiles were mapped between 0.5 mm and 45.0 mm above the burner surface. Mole fraction profiles were moved 0.9 mm (5 times the orifice diameter) towards the burner surface to account for probe perturbations. The temperature profile and area-expansion ratio were measured in the first study [17].

Calibration uncertainties affect the comparison of profiles. Among the C_3 's, propene (C_3H_6) was calibrated directly, and C_3H_4 in the allene-doped flame was calibrated directly with allene. Other species were calibrated by the method of relative ionization cross-sections, C_3H_2 and C_3H_3 relative to C_3H_4 , and C_3H_5 relative to C_3H_6 , and C_3H_4 in the undoped flame (a mixture of propyne and allene) relative to C_3H_6 . Direct calibration has an uncertainty of <10%, while the indirect calibration should be within a factor of two.

The surprise is that C_3H_3 remains constant within experimental uncertainty (Fig. 1), while C_6H_6 rises more than an order of magnitude ($\times 20$) in the allene-doped flame. C_6H_6 also peaks almost 4 mm earlier than propargyl and 3 mm earlier than its maximum in the undoped flame, which had been almost at the same position as that of propargyl.

Roughly, if propargyl were the sole reactant making benzene higher by a factor of twenty, we would have expected its mole fraction to be higher in the doped flame by a factor of 4-5 (square root of 20), but it is unchanged. A difference in rate of benzene destruction would affect this simple analysis. However, the temperatures and the mole fractions of H, O, and OH hardly change at all, so the oxidative environment for C_6H_6 is unchanged. Another contribution might be $C_3H_3+C_3H_4$ reaction, seeing that C_3H_4 is high and C_3H_3 is unchanged before the peak in C_6H_6 , but the C_3H_4 mole fractions would have to be a factor of twenty higher in this region, and they are not.

A second interesting observation is that mass 41, assigned to C_3H_3 , peaks at the same position as C_6H_6 (Fig. 2). Mass 41 probably has some contribution from $HCCO$, as mass 42 appears to be dominated by CH_2CO rather than C_3H_6 . However, modeling implies that allyl and 2-propenyl

are formed easily from H+allene, and we propose that CH_2CO is formed from the chemically activated reaction $\text{O}+\text{allene} = \text{H}+\text{CH}_2\text{CO}$.

Table 1. Species measured in low-pressure flat flames of ethene/oxygen/50.0% argon and 0.50% propadiene/ethene/oxygen/49.7% argon at fuel-rich ($\phi=1.90$) conditions.

| Species | Ethene | Propadiene/ethene | Species | Ethene | Propadiene/ethene |
|------------------------|---------|-------------------|--|----------|-------------------|
| H | Profile | Profile | CH_2CO | Profile* | Profile |
| H_2 | Profile | Profile | $\text{CH}_2\text{CHO}^{**}$ | Profile | Profile |
| CH_2 | Profile | Profile | CH_3CHO | Profile | Profile |
| CH_3 | Profile | Profile | CO_2 | Profile | Profile |
| CH_4 | Profile | Profile | C_4H_2 | Profile | Profile |
| OH | Profile | Profile | C_4H_3 | - | Profile |
| H_2O | Profile | Profile | C_4H_4 | Profile | Profile |
| C_2H_2 | Profile | Profile | C_4H_5 | - | Profile |
| C_2H_3 | Profile | Profile | C_4H_6 | - | Profile |
| C_2H_4 | Profile | Profile | $\text{C}_3\text{H}_3\text{O}/\text{C}_4\text{H}_7$ | - | Profile |
| CO | Profile | Profile | $\text{C}_3\text{H}_4\text{O}/\text{C}_4\text{H}_8$ | Profile | Profile |
| HCO | Profile | Profile | $\text{C}_3\text{H}_6\text{O}/\text{C}_4\text{H}_{10}$ | Profile | Profile |
| H_2CO | Profile | Profile | C_3H_4 | Profile | Profile |
| O_2 | Profile | Profile | C_3H_6 | Profile | Upper bound |
| HO_2 | - | Profile | $\text{C}_4\text{H}_3\text{O}/\text{C}_3\text{H}_7$ | Profile | Upper bound |
| H_2O_2 | - | Profile | $\text{C}_4\text{H}_4\text{O}/\text{C}_3\text{H}_8$ | Profile | - |
| C_3H_2 | Profile | Profile | $\text{C}_4\text{H}_6\text{O}/\text{C}_3\text{H}_{10}$ | Profile | - |
| C_3H_3 | Profile | Profile | $\text{C}_4\text{H}_8\text{O}/\text{C}_3\text{H}_{12}$ | Profile | - |
| C_3H_4 | Profile | Profile | C_6H_2 | Profile | Profile |
| Ar | Profile | Profile | C_6H_4 | Profile | Profile |
| HCCO | - | Postflame profile | C_6H_5 | Profile | Profile |
| C_3H_5 | Profile | Profile | C_6H_6 | Profile | Profile |

*Reported previously as C_3H_6 . **Possibly CH_2CHO^+ ionization fragment of CH_3CHO .

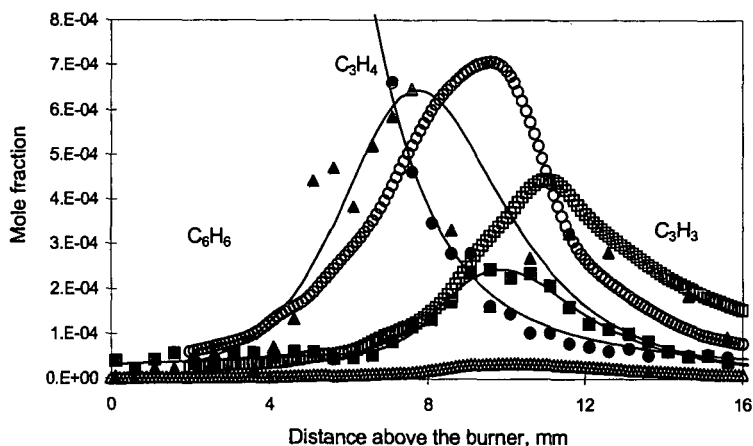


Figure 1. Species profiles in the ethene flames, undoped (open symbols) and allene-doped (filled symbols and lines): C_3H_4 (circles), C_3H_3 (squares) and C_6H_6 (triangles) in ethene flames.

Allyl has long been proposed as a precursor to benzene [18]. Stoichiometry works against it, though; its combination product C_6H_{10} has much hydrogen to lose. Also, it is not cyclic, and the weak allyl-allyl bond donates little energy for subsequent chemically activated reactions of C_6H_{10} .

Other explanations could be that mass 78 might not be benzene or that benzene is a side product formed from phenyl. Ionization potentials are the basis of identification. They match literature values well for benzene and phenyl, although the IP measurement with electron-impact ionization is not so precise as to distinguish them definitively among hydrocarbon isomers. In the allene-doped flame, phenyl reaches its maximum slightly before benzene (Fig. 2). It is a factor of 10 higher and occurs 2.5 mm earlier than in the undoped flame.

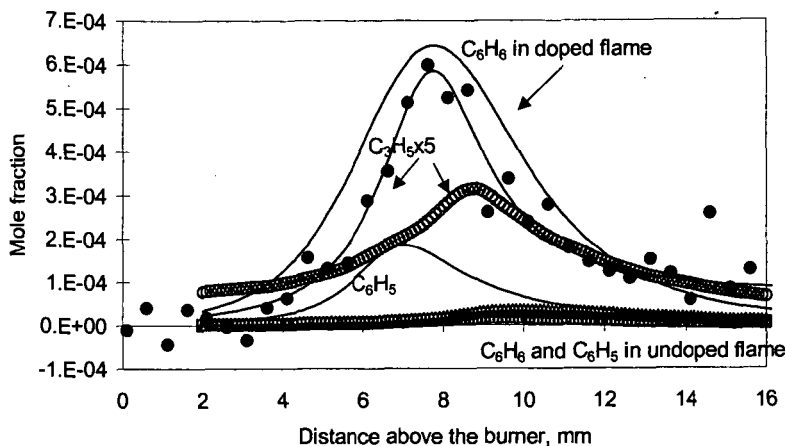


Figure 2. Species profiles in the ethene flames, undoped (open symbols) and allene-doped (filled symbols and lines): C_3H_3 (circles), C_6H_5 (squares), and C_6H_6 (triangles) in ethene flames.

C_4H_3 and C_4H_5 additions to C_2H_2 seem fairly plausible ways to reach aromatics here. Maximum mole fractions occur for C_2H_2 at 9 mm; C_3H_3 at 8.5 mm; C_4H_3 at about 9.5 mm; and C_4H_5 at 7 mm. All these are in the neighborhood of the C_6H_6 maximum. The C_4 radical peaks are both an order of magnitude higher in the doped flame.

CONCLUSIONS

There is strong evidence in many systems that propargyl combination is an important route to forming single-ring aromatics. It does not appear to explain the changes in benzene formation comparing MBMS profiles in a fuel-rich ethane flame with those in a near-identical flame doped with a small amount of allene. In the allene-doped flame, C_4H_3 and C_4H_5 routes may be dominant, despite the potential of allene as a C_3H_3 precursor.

With the correct kinetics, likely to be worked out in the next ten years, we will be able to use soot prediction from flame modeling for engineering analysis and design. To predict soot formation, we must be able to model flames of all sorts of fuels. There is no reason to think that propargyl combination should be the sole route to make aromatics, although it may often be the dominant one. Modeling of these and other flames will be used as an aid to interpreting the roles of the different routes, and new approaches are being applied to tighten the uncertainty of calibration factors.

ACKNOWLEDGEMENT

We gratefully acknowledge the support of the US Department of Energy, Basic Energy Sciences / Chemical Physics for support of this work under grant DE-FG02-91ER14192.

REFERENCES

1. Wagner, H.Gg., *18th Symposium (International) on Combustion*, The Combustion Institute, Pittsburgh, 1 (1980).
2. Frenklach, M., D.W. Clary, W.C. Gardiner, Jr., and S.E. Stein, *20th Symposium (International) on Combustion*, The Combustion Institute, Pittsburgh, 887 (1984).
3. Westmoreland, P.R., A.M. Dean, J.B. Howard, and J.P. Longwell, *J. Phys. Chem.* **93**, 8171-8180 (1989).
4. Cole, J.A., J.D. Bittner, J.B. Howard, and J.P. Longwell, *Combustion and Flame* **56**, 51 (1984).
5. Stehling, F.C., J.D. Frazee, and R.C. Anderson, *Sixth Symposium (International) on Combustion*, The Combustion Institute, Pittsburgh, 247 (1956).
6. Wu, C.H.; Kern, R.D. *J. Phys. Chem.* **91**, 6291 (1987).
7. Kern, R.D.; Singh, H. J.; Wu, C.H. *Int. J. Chem. Kin.* **20**, 731 (1988).

8. Thomas, S.D.; Westmoreland, P.R. "Role of C_3H_3 in Aromatics and Soot Formation," Paper 130g, 1989 Annual Meeting of AIChE, San Francisco CA, November 5-10, 1989.
9. Thomas, S.D., F. Communal, P.R. Westmoreland, " C_3H_3 Reaction Kinetics in Fuel-Rich Flames," *Preprints of Div. of Fuel Chemistry*, American Chemical Society, **36**, No. 4, 1448-1455 (1991).
10. Stein, S.E., J.A. Walker, M.M. Suryan, A. Fahr, *23rd Symposium (International) on Combustion*, The Combustion Institute, Pittsburgh, 85 (1991).
11. Alkemade, U., K.H. Homann, *Z. Phys. Chem. N.F.* **161**, 19 (1989).
12. Miller, J.A., R.J. Kee, C.K. Westbrook, *Ann. Rev. Phys. Chem.* **41**, 345 (1990).
13. Melius, C.F., J.A. Miller, E.M. Evleth, *24th Symposium (International) on Combustion*, The Combustion Institute, Pittsburgh, 621 (1992).
14. Wang, H., M. Frenklach, *Comb. Flame* **110**, 173 (1997).
15. Marinov, N.M., W.J. Pitz, C.K. Westbrook, A.M. Vincitore, M.J. Castaldi, S.M. Senkan, C.F. Melius, *Comb. Flame* **114**, 192 (1998).
16. Oulundsen Jr., G.E., "Measurements and Kinetics for Hydrocarbon-Chlorine and Allene-Doped Ethylene Flames," Ph.D. dissertation, Chemical Engineering, U. Massachusetts (2000).
17. Bhargava, A., P. R. Westmoreland, *Combustion and Flame* **113**, 333 (1998).
18. Kinney, R.E., D.J. Crowley, *Ind. Eng. Chem* **46**, 258 (1954).

MICROWAVE DESTRUCTION OF TRICHLOROETHYLENE IN A H₂O - O₂ - AR PLASMA

Yongsam Ko¹, GoSu Yang², Daniel P. Y. Chang³ and Ian M. Kennedy⁴

¹ Department of Environmental Engineering, Yosu National University, Korea

² Department of Mechanical Engineering, Chonbuk National University, Korea

³ Department of Civil and Environmental Engineering, University of California Davis

⁴ Department of Mechanical and Aeronautical Engineering, University of California Davis

INTRODUCTION

As of 1997, total U. S. emissions of volatile organic compounds (VOC) had fallen to an estimated 19×10^6 tpy (tons per year) while total NO_x emissions continued to rise to about 24×10^6 tpy¹. Among VOC categories, solvent usage increased to roughly to 6.5×10^6 tpy². Of especial concern are those compounds that are toxic air contaminants (TAC), or that may produce toxic by-products while undergoing capture and treatment. Chlorinated solvents, chlorofluorocarbons and sulfur hexafluoride fall into such a category because of their higher activation energies and low biodegradability under oxidative conditions. In terms of millions of U.S. tons of carbon equivalents, i.e., a measure of greenhouse gas potential, an increase of about 67% (16×10^6 tpy) has occurred in the emissions of HCFCs, PFCs, and SF₆ during the decade of the 1990's². Although increases in emissions have occurred, concentrations of emitted streams may actually be decreasing because of improved production methods or capture of these pollutants. Control costs generally increase as concentrations decrease, e.g., the cost of catalytic incineration of VOCs increases from about \$5,000/ton to \$50,000/ton for a compound such as benzene as its concentration drops from 100 ppm, to 10 ppm, resulting in even the least costly of combustion control measures impractical for low concentration streams. Control costs for NO_x range from roughly less than about \$1000/ton for advanced burner technologies to over \$5,000/ton for exhaust gas treatments³. Development of efficient control strategies for low concentrations of these compounds while avoiding NO_x formation is highly desirable.

Conventional methods for removing volatile organic compounds (VOC's) from gas streams include absorption, adsorption, condensation, and incineration (including thermal and catalytic). Among these technologies, adsorption is an efficient and economical method for moderate to low concentration streams. Nevertheless, adsorbates (such as VOCs) must be removed periodically after they saturate the adsorbents (e.g., activated carbon or zeolites) and require further treatment.

There are two conventional regeneration methods: steam and hot gas regeneration. The former requires a steam generation facility while leaving the adsorbent bed wet with condensate, thus requiring that time and equipment be available to dry out the bed before its reuse. Moisture in the condensate can also lead to undesirable chemical reactions between the VOCs and bed materials. Regeneration with a hot gas is accomplished by heating the adsorbent (and adsorbate) to a temperature sufficient to desorb the adsorbate. The flow of hot gas not only heats the adsorbent, but also purges the adsorbate as it is desorbed resulting in a lower final concentration factor. Effective adsorbents also create a problem in regeneration, since generally, the more effective the adsorbent the more difficult it is to remove the adsorbate. Thus, a long regeneration time and large purge gas volumes are required. Moreover, the heating requirements are large since not only the adsorbent, but also the adsorbent support, the adsorbent column, associated conduits and the purge gas itself often must be heated. If a higher temperature purge gas was used, the desorption could be more rapid, but thermal degradation could yield undesirable intermediate by-products and shorten the life of the adsorbent reducing its capacity. In the case of activated carbon the potential for a fire exists.

Microwave regeneration utilizes "dielectric heating" which eliminates many of the above drawbacks and provides benefits unobtainable with conventional regeneration. In the microwave regeneration process, heat is generated internally, i.e., within the adsorbent bed either by heating the adsorbate directly and/or the adsorbent. It does not need to be conveyed through a fluid; therefore a minimal amount of purge gas is used and large concentration factors can be obtained. Minimal heating of ancillary mass occurs, reducing over all energy requirements and cooling time. As a result, a microwave regeneration process makes it possible to desorb VOCs from adsorbents rapidly and efficiently. In addition, the microwave system can be used for the destruction of the desorbed waste stream.

Microwave technology for waste treatment

Plasma processing for environmental remediation applications is a developing technology. The primary interest in plasma processes has been in the area of combustion, due to the ability to generate extremely high temperatures, approaching 10,000 K, in the gas phase. By comparison,

most chemical thermal processes, such as incineration, operate at temperatures ranging from 2000 to 2500 K. The higher temperatures attainable in a plasma process minimize the potential for the *in situ* formation of polynuclear aromatic hydrocarbons (PAH), dioxins and furans, that are major concerns of incineration processes. The cooling of a plasma is rapid and not conducive to molecular growth processes that yield complex molecules. However, thermal systems that are operated with air suffer from a common problem - the production of oxides of nitrogen (NO_x).

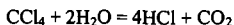
Recently there has been a growing interest in potential applications of high-frequency plasmas. For example, Wang et al.⁴ reported the use of a RF plasma system to convert dichlorodifluoromethane to methane and acetylene in a hydrogen environment. Microwave plasmas may also be applied to the remediation of off-gas streams. Microwave plasmas possess a number of advantages over plasmas generated by other types of electrical excitation which make them attractive for this application: (1) production of high ionization levels and molecular dissociation without excess heating of the contained gas; (2) construction of reaction vessels which are simple, free from contamination and less subject to damage because of the absence of internal electrodes; (3) production of little electrical interference; (4) absence of high voltages which can be easily contacted by operating personnel, i. e., absence of shock hazardous; (5) potentially lower power consumption; (6) and the ability to tolerate high concentrations of water. The latter feature is particularly important because it means that energy can be fed directly into a flow with high water concentration and a stable plasma can be established.

Although the microwave plasma process has been successfully applied in the metals⁵ and microelectronics industries⁶, the application of microwave plasma technology to hazardous waste treatment is very limited. Bailin et al.⁷ first investigated the decomposition of organic compounds by passage through a microwave-induced oxygen plasma. The basic idea in their study was to apply microwave discharge energy to break chemical bonds of organic compounds under reduced pressure conditions. Hertzler et al.⁸ oxidized halocarbons with molecular oxygen directly in a low-pressure tubular flow microwave plasma discharge reactor. Although conversion of parent compounds exceeded 99.99%, a complete product analysis was not provided, and, therefore effluent toxicity could not be determined. Moreover, in the above studies, the organic compounds were introduced in liquid form into the plasma reactor. In other words, a microwave plasma was used to treat liquid organic wastes.

Researchers in Japan have been particularly active in promoting plasma technology for waste remediation. They have included microwave plasma systems in their studies. Suzuki et al.⁹ investigated the use of a microwave heated oxygen plasma for the conversion of metal chlorides into oxides. The method was shown to be successful in the conversion of a wide range of metals, from transition metals to lanthanides, with results that were consistent with an equilibrium analysis. Shimizu et al.^{10, 11} studied the decomposition of trichlorotrifluoroethane with a microwave induced argon plasma. They used SiC fibers to assist in the generation of the plasma. The plasma was operated at one atmosphere pressure with small amounts of O₂ added to ensure complete conversion of C to CO₂. Somewhat surprisingly, they found that pulsed microwave operation achieved better destruction of the waste feed than DC operation. However, the reason for this behavior was not discovered.

Chlorine that is present in waste materials is most conveniently sequestered as HCl. When Cl is bonded to H it is effectively removed from participation in all further reactions, except at very high temperatures. Ultimately, HCl needs to be handled with devices such as wet scrubbers where it can be neutralized. Dechlorination of wastes is an important first step in reducing the toxicity of remediation by-products through the prevention of formation of compounds such as tetra-chloro-dibenzo-dioxin (TCDD).

The dechlorination of these compounds is thermodynamically favored by reaction in a reducing environment. Barat and Bozzelli¹² showed that an overall reaction of the form



exhibited large equilibrium constants

| T, K | K _p |
|------|------------------------|
| 300 | 3.8 x 10 ⁴³ |
| 800 | 7.6 x 10 ²⁵ |

When oxygen is present in the system, O competes with Cl for bonding with H atoms. Hence, the ideal conditions for dechlorination are reducing, not oxidative. Barat and Bozzelli used a quartz flow reactor, driven by a microwave plasma, to examine the reaction of H₂ and H₂O with chlorocarbons. Reactions with H₂ yielded non-parent chlorocarbons, low molecular weight hydrocarbons, and soot. Reactions with water yielded only carbon monoxide and carbon dioxide.

The production of carbon monoxide was a necessary side effect of the stoichiometry that was used; insufficient oxygen was available to ensure complete oxidation of the available carbon. Ravindran et al.¹³ have shown from thermodynamic arguments that a similar dechlorination in hydrocarbon rich environments is also possible.

EXPERIMENTAL

A continuous microwave generator (low ripple magnetron, 1.5 KW, 2450 MHz; Gerling Laboratory) and a plasma tuner (ASTEX) were used to generate a steam plasma. A schematic diagram illustrating the gas flow paths is shown in figure 1. The main components of the system consisted of a plasma reactor (AX 7200), a plasma tuner, microwave generator and microwave wave-guide. Continuous microwave power from the magnetron was conducted through a waveguide to the plasma torch. The forward and reflected powers from the plasma torch could be maximized and minimized by adjusting the tuning stubs on the plasma tuner. The forward power was maintained at 600W and the reflected power was maintained below about 100 W. The plasma reactor consisted of a 1/4" O.D. ceramic tube through which the mixture to be reacted was passed, and an outer quartz tube housing.

Argon, oxygen and steam were used as gases from which a plasma was generated. The Ar was utilized as a basic carrier and reference gas, the O₂ provided stoichiometric oxidation requirements for the chlorinated hydrocarbon tested and steam provided a reactive atmosphere containing additional hydrogen. Steam was generated by a coiled-tubing heater and was carried by Ar gas. All plasma gas flow rates were controlled by rotameters meters and were introduced to the plasma torch as shown in Figure 1. The total flow rate of gases was held constant at 10 lpm. The proportion of steam was established by trial-and-error to obtain an intense plasma. All the lines from the flow meter to the torch were heated to prevent steam condensation.

A solvent, trichloroethylene (TCE) was selected as the target compound and introduced through the ceramic tube in the plasma reactor. Destruction and removal efficiency (DRE) for TCE was calculated from measured concentrations remaining and the known flow rates to determine the efficiency of the steam plasma. The effluent gas from the plasma reactor was passed through two traps. The first trap consisted of a coiled water concentrator and an Erlenmeyer flask, in which the most of the steam was condensed. A second back-up trap was used to condense the remaining water vapor. Gas samples were collected on an adsorbent bed of Carbotrap C. A gas sampling loop and switching valve were used to inject gas samples to the GC from a by-pass line exiting the second trap. Liquid samples were also collected from the first and the second traps. The reactor effluents were analyzed with an on-line GC equipped with a TCD detector (TCE) and by GC/MS (adsorbent tubes - TCE and other by-products), and a specific ion meter for chloride. The Carbotrap samples were Soxhlet extracted for 20 hours with methylene chloride with deuterated phenanthrene and terphenyl added as internal standards. The samples were evaporated down to 0.5 mL prior to injection into a HP GC/MS system.

RESULTS AND DISCUSSION

The DRE for TCE was evaluated in the microwave system for a series of microwave powers at a condition of 30% steam with an O₂ flow rate of 0.5 lpm and an argon flow rate of 6 lpm. The concentration of TCE in the input flow to the plasma was 1700 ppm. The small amount of O₂ was added to ensure that sufficient O₂ was available in the system to complete the oxidation of TCE. The post plasma gases were analyzed on a GC. The results are shown in Table 1.

Table 1. DRE and Cl⁻ ion concentration in post plasma gases at different operating powers

| Power (W) | DRE (%) | Cl ⁻ (ppm) |
|-----------|---------|-----------------------|
| 200 | 58 | 10800 |
| 300 | 99.8 | 38700 |
| 400 | 100 | 52000 |
| 500 | 100 | 56200 |
| 600 | 100 | 56900 |

It is apparent that the plasma system is quite capable of achieving significant destruction at operating powers as low as 400 W. The chloride ion concentration is a measure of the HCl that is formed and is second measure of the accuracy of the sampling system and analysis. The constant Cl⁻ concentration at powers above 400 W confirms the conclusion that all the input chlorine was sequestered as HCl under these conditions.

Experiments were also conducted with a power of 600 W and a TCE input concentration of 1700 ppm but with varying concentrations of steam in the plasma. The results of those tests are shown in Table 2.

The presence of steam is seen to have an important impact on the effectiveness of the microwave destruction process. The effect of steam that is shown in Table 2 is consistent with the observation of Barat and Bozzelli that at the temperatures of the microwave plasma, thermodynamics favors the dechlorination of chlorinated hydrocarbons.

Finally, the Carbotrap samples were analyzed on a GC/MS system for products of incomplete combustion. The microwave power was 600 W with 30% steam and 1700 ppm of TCE. This analysis did not find any evidence of dioxins or furans, showing that a high DRE can be achieved without the production of other products of incomplete reaction.

Table 2. DRE at 600 W of input microwave power with varying steam concentrations

| Steam fraction of flow (%) | DRE |
|----------------------------|-------|
| 0 | 99.78 |
| 5 | 99.9 |
| 10 | 100 |
| 20 | 100 |
| 30 | 100 |

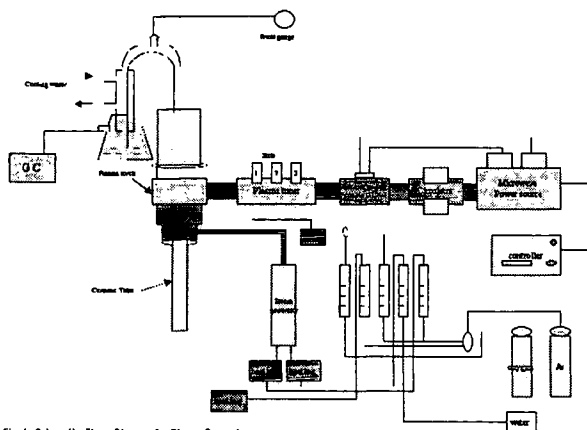


Fig. 1 Schematic Flow Diagram for Plasma Generator

REFERENCES

1. U.S. EPA, National air pollutant emission trends: 1900 - 1998, Technology transfer network chief database, <http://www.epa.gov/ttn/chief> (2000).
2. U.S. EPA, Inventory of U.S. Greenhouse gas emissions and sinks: 1990 - 1997, technology transfer network chief database, <http://www.epa.gov/ttn/chief> (1999).
3. U.S. EPA, Cost-effective nitrogen oxides (NO_x) reasonably available control technology (RACT). Memorandum from D. Kent Barry, Air Quality management Division, Office of Air Quality Planning and Standards, Washington D.C., (1994).
4. Wang, Y., Lee, W., Chen, C. and Hsieh, L., Decomposition of dichlorodifluoromethane by adding hydrogen in a cold plasma system, *Environmental Science and Technology*, **33**, 2234-2240 (1999).
5. Zanetti, R. J., *Chemical Engineering*, **90**, 14-16 (1983).
6. Fraser, D. B., Westwood, W.D. (1990) in , , Eds., *Handbook of plasma processing technology*, in (eds. S. M. Rossmagel, J. J. Cuomo and W. D. Westwood), Noyes Park Ridge, NJ (1990).
7. Bailin, L. J. and Hertzler, B. L., *Detoxification of pesticides and hazardous wastes by the microwave plasma process*, ACS Symposium Series 73 Chicago, August 29 - September 2. (1977).
8. EPA, Development of microwave plasma detoxification process for hazardous wastes (phase iii), (1979).

9. Suzuki, M., Komatsubara, M., Umebayashi, M. and Akatsuka, H., Conversion of chloride waste into oxide by microwave heated oxygen plasma, *Journal of Nuclear Science and Technology*, **34**, 1159-1170 (1997).
10. Shimizu, Y., Ogawa, K., Takao, Y. and Egashira, M., Decomposition of trichloroethylene by microwave-induced ar plasma generated from SiC ceramics under atmospheric pressure, *Denki Kagaku*, **66**, 1018-1025 (1998).
11. Shimizu, Y., Akai, Y., Hyodo, T., Takao, Y. and Egashira, M., Decomposition of trichlorotrifluoroethane by microwave-induced ar plasma generated from SiC ceramics under atmospheric pressure, *Journal of the Electrochemical Society*, **146**, 3052-3057 (1999).
12. Barat, R. B. and Bozzelli, J. W., Reaction of chlorocarbons to HCl and hydrocarbons in a hydrogen-rich microwave-induced plasma reactor, *Environmental Science Technology*, **23**, 666-671 (1989).
13. Ravindran, V., Pirbazari, M., Benson, S. W., Badriyha, B. N. and Evans, D. H., Thermal destruction of chlorinated hydrocarbons by reductive pyrolysis, *Combustion Science Technology*, **122**, 183-213 (1997).

ZEOLITE-BASED MERCURY SORBENT- LABORATORY TESTING AND MODELING

Thomai Panagiotou, Joseph R. Morency and Constance L. Senior

Physical Sciences Inc., 20 New England Business Center, Andover, MA 01810

KEYWORDS: mercury removal, zeolites, air pollution

INTRODUCTION

Mercury is one of the 11 toxic metals recognized by the Title III of the Clean Air Act Amendments as Hazardous Air Pollutants and has received special attention because of its high volatility combined with high toxicity and bioaccumulation. In the United States 21% of the total mercury emissions are attributed to coal-fired utility boilers.¹ The forms of mercury vapor in power plant flue gases are elemental Hg and oxidized Hg (probably HgCl_2 , and in some cases, HgO), with elemental mercury being the predominant form.²⁻⁶ Generally, HgCl_2 can be removed from the flue gases easier than elemental Hg, either through wet scrubbing, dry injection or fixed bed using activated carbon.³⁻¹⁰ However, removal of elemental mercury is more challenging, since it is practically insoluble in water and can be removed to a certain extent with expensively treated activated carbons

PSI has developed and tested mercury sorbents for enhanced removal of both elemental and oxidized mercury based on a natural zeolite. The sorbents were injected to mercury containing flue gases from combustion of coal, which were at 150 or 230°C. Three different forms of this zeolite were used, plain zeolite and two types of modified zeolites treated with proprietary agents.

EXPERIMENTAL

Combustion of coal took place at PSI's electrically heated Entrained Flow Reactor (EFR). This apparatus, which can achieve a maximum gas temperature of 1723 K, has been used extensively on many of PSI's combustion research projects. Fuel, air, other gases and coal are injected at the top of the reactor. The combustion section is an externally heated ceramic tube that is 8.57 cm in internal diameter and 158 cm in length.

Once the flue gas exited the furnace, it entered a quartz tubular reactor where sorbent injection took place. The reactor temperature was kept constant to 130 or 200°C. To ensure that no additional mercury removal took place downstream the reactor, the flue gases passed through a series of particulate removal devices, including an impactor, two cyclones and finally a filter, see Fig. 1. The particle removal devices were kept at about 150°C.

After leaving the filter assembly, the gas stream passed into a series of impingers designed to collect any mercury left in the flue gases and determine the mercury species, as specified by Ontario Hydro Method. The sorbent injection system consisted of a syringe with the sorbent loaded on driven by a syringe pump into a tube. The air flowing in the tube was used to carry the sorbent. The injection rate was controlled by the speed of the syringe pump.

Coal was burned in the EFR to more closely approach the conditions found in power plant flue gases. For this program, a bituminous coal, Pittsburgh seam, was used. The mercury content of the coal as determined by Neutron Activation Analysis is 0.11 ppm. To maintain 10-70 $\mu\text{g}/\text{m}^3$ levels of Hg concentration, a mercury laden stream of oxygen was added to the top of the EFR.

Two types of treated zeolite were used, TZ1 and TZ2, and also untreated zeolite, UZ, with particle size in the range of 1 to 5 μm . In addition, a high-surface-area activated carbon, AC, CL-213, from Barneby and Sutcliffe was used as a comparison.

The normal operating conditions were:

- Coal flow rate: 1.7 g/min
- Furnace temperature: 1700 K
- Equivalence ratio: 1.2
- Mercury reactor residence time: 2-3 s
- Mercury reactor temperature: 130 and 230°C.

At the end of each experiment six samples were collected and analyzed for mercury concentration: the ash/sorbent from the impactor and the two cyclones, the filter with any collected material, the three liquid samples from the Ontario-Hydro sampling train and the rinse of the glassware.

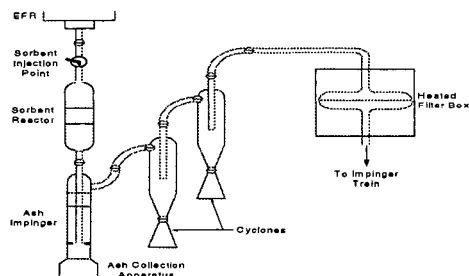


Figure 1. Sorbent injection, reactor and particulate collection apparatus for sorbent injection experiments.

RESULTS

Sorbent Injection Data

Figure 2 shows a plot of mercury capture as a function of sorbent:Hg ratio. For all sorbents capturing efficiency increased with sorbent to mercury ratio. The removal efficiencies of a treated zeolite (TZ2) and activated carbon (AC) were well over 90% even for modest sorbent to Hg ratios in the range of 25,000. The other treated zeolite (TZ1) exhibited removal efficiencies 45-55% for average sorbent to mercury ratios and up to 85% for high sorbent to mercury ratios, of about 90,000. The temperature did not appear to affect the capturing efficiency of the sorbents.

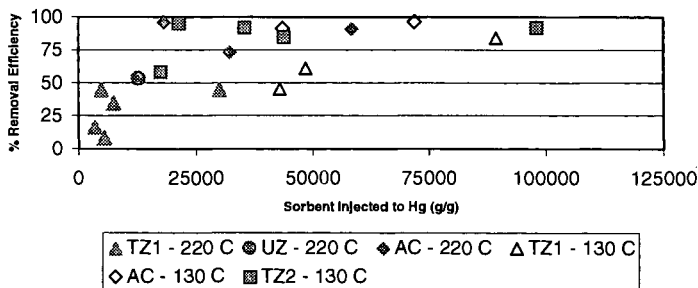


Figure 2. Mercury removal efficiency as a function of sorbent to mercury ratios.

Figure 3 shows the amount of mercury removed per unit mass of sorbent (sorbent utilization) plotted against the sorbent to mercury ratio present in the effluent stream. As the sorbent to mercury ratio increases, the amount of mercury removed per unit mass of sorbent decreases for all sorbents.

Figure 4 shows the percentage of oxidized mercury in the remaining mercury (was not removed by the sorbents) as a function of sorbent to mercury ratio. For low sorbent to mercury ratios, oxidized mercury decreases from 25% to less than 5% at a sorbent to mercury ratio of 25,000. Then it increases to about 50% for a sorbent to mercury ratio of 50,000 and decreases to less than

Mercury mass balance closure was determined for all runs by adding the mercury from each of the analyzed samples and dividing by the sum of the theoretical mercury from the combustion of the coal and the added mercury from the permeation tube as determined by the Jerome analyzer. The mercury mass balance for most of the runs was in the range of 70-110%.

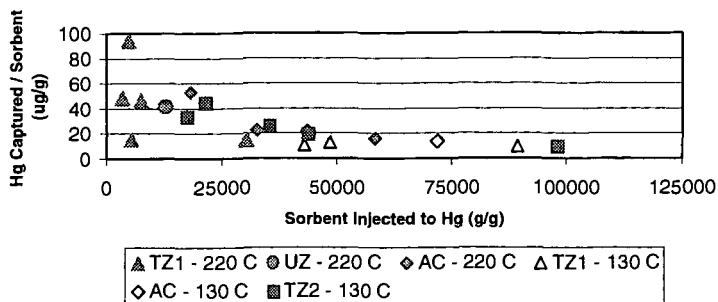


Figure 3. Sorbent utilization as a function of sorbent to mercury ratio.

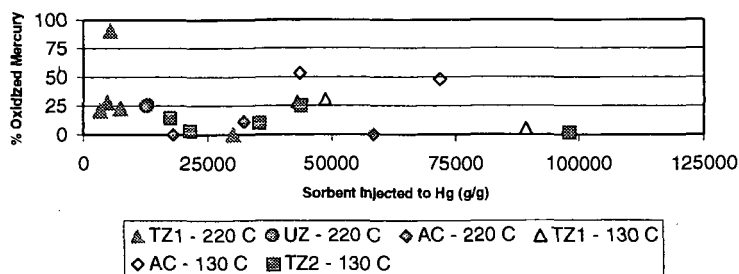


Figure 4. Percentage of oxidized mercury in the remaining (not removed) mercury.

Baseline Runs

In order to characterize the experimental apparatus and explain experimental data, three types of baseline runs were conducted. In all cases additional mercury was added to the system.

- (A) No coal combustion took place and no sorbent was injected. The purpose of these experiments was to determine the amount of mercury that may be lost while flowing through the furnace.
- (B) No coal combustion took place but treated zeolite was injected. The purpose of these experiments was to determine the amount of mercury captured by the treated zeolite when no coal combustion products are present.
- (C) Coal combustion took place but no sorbent was injected. The purpose of these experiments was to measure the amount of mercury removed by the fly ash alone.

For baseline A runs, over 98% of the total amount of mercury injected is recovered in the impingers at the end of the baseline A runs. This indicates that there is no substantial amount of mercury lost or unaccounted for while flowing through the furnace. Also for these runs, greater than 95% of the mercury is collected as elemental mercury.

In baseline type B, TZ1 was injected into the sorbent reactor at 130°C (266°F), with no coal combustion taking place. The sorbent to Hg ratio was 89,000 and the removal efficiency was 85 %. Similar removal efficiencies of the same sorbent were found in presence of combustion products, see Fig. 2.

Removal efficiencies from ash, as measured in baseline C runs (ash baseline) are shown in Fig. 5. Removal efficiencies increase from about 35% to 65% as the ash to mercury increases from 50,000 to 120,000.

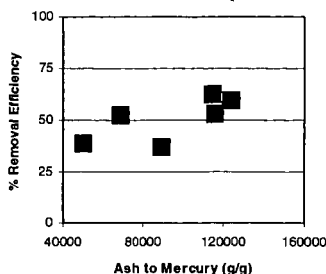


Figure 5. Ash removal efficiency as a function of ash to mercury ratio.

Modeling

The impact of speciation of mercury on activated carbon performance has been quantified in laboratory fixed bed experiments¹¹ and these data can be applied to models for the performance of sorbents in duct injection mode.¹² Figure 6 shows a calculation of the mercury removal at 130 °C for 5 micron activated carbon particles and a mercury concentration of 35 $\mu\text{g}/\text{m}^3$. The calculation assumes plug flow conditions with a two second residence time. Using fixed bed data to determine the reactivity of a single activated carbon to elemental mercury and mercury chloride, the figure shows the removal efficiency for both species. Mercury chloride shows a higher removal rate for a fixed sorbent to mercury ratio. Figures 2 and 6 show a good agreement between theory and experiments.

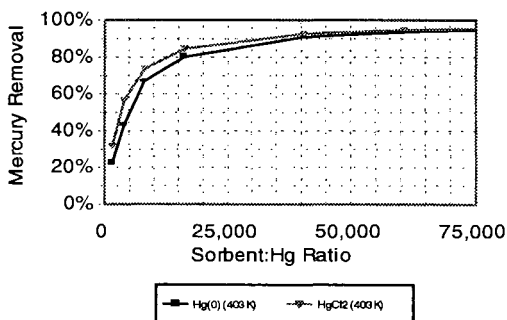


Figure 6. Calculated mercury removal for 2 seconds residence time at 130°C, assuming 5 micron activated carbon and concentration of 35 $\mu\text{g}/\text{m}^3$.

DISCUSSION

The ash baseline runs, see Fig. 5, indicate that ash can remove substantial amounts of mercury, as long as sorbent is not present. However, in the presence of sorbent, ash appears to lose its ability to remove mercury. If we assume that the removal efficiency of ash is independent of the presence of sorbent, then the removal efficiencies in presence of sorbent would have to be much higher than those indicated in Fig. 2.

Results indicate that oxidation of mercury takes place in presence of ash and/or sorbent. Baseline A suggests that only 5% of the injected mercury is oxidized in the furnace when no combustion products are present. However, in the presence of combustion products and/or sorbents, oxidized mercury can be 25-50% of the remaining (not removed) total mercury. Taking into account the removal efficiency, there is a net production of oxidized mercury from elemental in those experiments.

Physical Sciences Inc. (PSI) is developing mercury sorbents using a zeolite material treated with proprietary agents for improved capture of elemental as well as oxidized mercury. The performance of these sorbents was compared with that of activated carbon tested at similar conditions. To identify removal mechanisms of mercury, the mercury removal process was modeled using an adsorption/diffusion model.

The mercury removal efficiencies of sorbents varied in the range of 45-96% for sorbent to Hg ratios in the range of 5,000-96,000. A treated zeolite (TZ2) and the activated carbon exhibited removal efficiencies well over 90% at modest sorbent to Hg injection ratios of 25,000. The sorbent utilization, expressed as the amount of mercury removed per unit mass of sorbent, decreased from 80 $\mu\text{g Hg/g}$ of sorbent to 6 $\mu\text{g Hg/g}$ of sorbent as the sorbent to Hg ratio increased from 5000 to 96,000. When no sorbent was injected, ash did remove some mercury, but in the presence of sorbent the role of ash in mercury removal appeared to diminish, presumably due to the higher reactivity of the sorbent with respect to the ash. Also, when no sorbent was present ash appeared to oxidize mercury, but in the presence of sorbent no substantial oxidation of mercury appeared to have taken place.

Results from the modeling effort suggest that at low sorbent injection rates mercury removal is highly influenced by adsorption kinetics. At higher concentrations diffusion becomes more pronounced. Also, modeling results indicate that most mercury is removed very shortly after injection, while long injection times do not substantially increase the removal rate.

ACKNOWLEDGMENTS

This work was supported by the Department of Energy under Grant # DE-FG02-97ER82456.

REFERENCES

1. *Mercury Study Report to Congress*, EPA-452/R-96-001g, 1996.
2. Tumati, P.R.; DeVito, M.S. "Partitioning Behavior of Mercury During Coal Combustion," presented at the Joint ASME/IEEE Power Gen. Conf., Kansas City, KS (October 1993).
3. DeVito, M.S.; Jackson, B.L. "Trace Element Partitioning and Emissions in Coal-Fired Utility Systems," presented at the 87th Annual Meeting and Exposition of the Air and Waste Management Association, Cincinnati, OH (June 1994).
4. Meij, R. "Distribution of Trace Species in Power Plant Streams: A European Perspective," presented at American Power Conf., Chicago (April 1994).
5. Nordin, A.; Schager, P.; Hall, B. "Mercury Speciation in Flue Gases: A Comparison of Results from Equilibrium Calculations with Results from Laboratory Experiments," Swedish Flame Days, Turku, Finland (September 1990).
6. Young, B.C.; Miller, S.J.; Laudal, D.L. "Carbon Sorption of Trace Mercury Species," proceedings of the 11th Annual Pittsburgh Coal Conference (September 1994), pp. 575-580.
7. Gorishi, B.; Gullet, B.K. "Sorption of Mercury Species by Activated Carbon and Calcium Based Sorbents: Effect of Temperature, Mercury Concentration and Acid Gases," *Waste Management & Research* **1998**, 6, 582-593.
8. Guijarro, M.I.; Mendioroz, S.; Munoz, V. "Effect of Morphology of Sulfurized Materials in the Retention of Mercury from Gas Streams," *Ind. Eng. Chem. Res.* **1998**, 37, 1088-1094.
9. Mendioroz, S.; Guijarro, M.I.; Bermejo, P.J.; Munoz, V. "Mercury Retrieval from Flue Gas by Monolithic Absorbents Based on Sulfurized Sepiolite," *Environ. Sci. Technol.* **1999**, 33, 1697-1702.
10. Karatza, D.; Lancia, A.; Musmarra, D. "Fly Ash Capture of Mercuric Chloride Vapors From Exhaust Combustion Gas," *Environ. Sci. Technol.* **1998**, 32, 3999-4004.
11. Carey, T.R., Hargrove, O.W., Richardson, C.F., Chang, R., and Meserole, F.B., "Factors Affecting Mercury Control in Utility Flue Gas Using Sorbent Injection," Paper 97-WA72A.05, presented at Air & Waste Management Association 90th Annual Meeting, June 8-13, 1997, Toronto, Ontario, Canada.
12. Meserole, F.B., Chang, R., Carey, T.R., Machac, J., Richardson, C.F., "Modeling Mercury Removal by Sorbent Injection," *J. Air Waste Manage. Assoc.*, **1999**, 49, 694-704.

PREDICTION OF MERCURY AIR EMISSIONS FROM COAL-FIRED POWER PLANTS

Constance L. Senior
Physical Sciences Inc.
20 New England Business Center
Andover, MA 01810

KEYWORDS: mercury, hazardous air pollutants, coal-fired power plant

INTRODUCTION

A recent report by the Environmental Protection Agency (EPA) on emission of hazardous air pollutants by electric utilities predicted that emissions of air toxics from coal-fired utilities would increase by 10 to 30% by the year 2010.¹ Mercury from coal-fired utilities was identified as the hazardous air pollutant of greatest potential public health concern. Anthropogenic emissions of mercury account for 10 to 30% of the world-wide emissions of mercury.² EPA has estimated that during the period 1994-1995 annual emissions of mercury from human activities in the United States were 159 tons.² Approximately 87% of these emissions were from combustion sources. Coal-fired utilities in the U.S. were estimated to emit 51 tons of mercury per year into the air during this period.

The form of mercury emitted from point sources is a critical variable in modeling the patterns and amount of mercury deposition from the atmosphere.^{1,3} Both elemental and oxidized mercury are emitted to the air from combustion point sources. Elemental mercury has a lifetime in the atmosphere of up to a year, while oxidized forms of mercury have lifetimes of a few days or less⁶ as a result of the higher solubility of Hg^{+2} in atmospheric moisture. Elemental mercury can thus be transported over long distances, whereas oxidized and particulate mercury deposit near the point of emission. Once mercury has deposited on land or water, it can transform into methylmercury, an organic form, and thereby enter the food chain. Humans are most likely to be exposed to methylmercury through consumption of fish.

Measurements of the concentration of mercury species taken in the stacks of pilot and full scale coal combustion systems show more than half of the vapor phase mercury as an oxidized form which is likely to be HgCl_2 . Current measurement methods cannot identify specific oxidized species of mercury.^{4,5} The range of observed values is broad: one study consisting of mercury speciation measurements from fourteen different coal combustion systems reported anywhere from 30% Hg^{+2} to 95% Hg^{+2} upstream of the air pollution control device (APCD).⁴

Although we can identify the major reaction pathways for mercury in coal combustion flue gas with some degree of confidence, we cannot yet make quantitative predictions of the emissions of specific mercury species from coal-fired power plants. The goal of this work is to advance the state of knowledge such that a predictive model for emissions of total mercury and for speciation of mercury can be formulated.

MERCURY EMISSIONS

A simple mass balance model for emissions of mercury from coal-fired power plants was devised to test our current understanding of mercury transformations in flue gas. The post-combustion region of the boiler was divided into three parts: 1) convective section to air heater (AH); 2) electrostatic precipitator (ESP); and 3) flue gas desulfurization unit (FGD). Concentrations of mercury species (gaseous and condensed) in each section were either calculated from equilibrium or plant parameters, or assigned based upon limited observations available from field data. All of the mercury is assumed to start as gaseous elemental mercury (Hg^0). In the AH section, elemental mercury can oxidize to Hg^{+2} , nominally the sum of HgO and HgCl_2 . In addition, both Hg^0 and Hg^{+2} can be adsorbed on particulate matter in the AH section, converting them to Hg_p . No change of mercury speciation or partitioning was calculated in the ESP because there are not enough data available to deduce mechanisms (or clear trends). In the FGD section, both Hg^0 and Hg^{+2} can be absorbed into the scrubber solution. In addition, a fraction of the adsorbed Hg^{+2} can be converted to gaseous Hg^0 . The model therefore predicts the speciation and emissions of mercury from the boiler based upon coal mercury content, equilibrium at elevated temperatures, assumed mercury partitioning coefficients in the various sections of the boiler, and scrubber operation as outlined in Table 1.

Recent DoE-sponsored field studies have been conducted to measure mercury speciation and mercury mass balances on coal-fired power plants using the Ontario Hydro method for gaseous mercury sampling. These data provide the best set for testing the model. In one study,⁸ six

power plants were sampled which all burned Eastern bituminous coal. The plants all had wet scrubbers and ESP's. In another study,⁹ a power plant burning a Western lignite was sampled. This plant also had a wet scrubber and an ESP.

Table 1. Mercury Model Parameters

| Parameter | Value | Notes |
|---|-------|--|
| Fraction of Hg^0 Oxidized in AH | ** | Calculated from Equilibrium at 825 K |
| Fraction of Hg^0 Adsorbed in AH | 0% | Assumed |
| Fraction of Hg^{+2} Adsorbed in AH | ** | Calculated from LOI for bituminous coals |
| Fraction of Hg^0 Oxidized in ESP | 0% | Assumed |
| Fraction of Hg^0 Adsorbed in ESP | 0% | Assumed |
| Fraction of Hg^{+2} Adsorbed in ESP | 0% | Assumed |
| Collection Efficiency of ESP | ** | Input from Plant Operation |
| Fraction of Hg^0 Absorbed in FGD | 0% | Assumed |
| Fraction of Hg^{+2} Absorbed in FGD | ** | Calculated from scrubber type and operating parameters |
| Fraction of Adsorbed Hg^{+2} Reduced to Hg^0 in FGD | ** | Calculated from scrubber type and operating parameters |

Since there is not currently enough information on the gas-phase reactions of mercury in flue gas, a simple approach was taken to predict the amount of mercury oxidation that takes place in the convective pass. When detailed kinetic information is available, this will be incorporated into the model. The amount of oxidation was calculated assuming that the chemical composition is frozen, equal to the equilibrium composition at 825 K. The results of equilibrium calculations at 20% excess air for a number of different coals were used to derive this correlation, shown in Figure 1. A range of chlorine contents, from 25 to 4500 ppm, were used in the calculation. At very low chlorine contents (< 50 ppm), most of the gas-phase oxidized mercury is predicted to be HgO . Many western fuels fall into this low-chlorine category. The adsorption behavior of HgO on fly ash may be different from HgCl_2 .

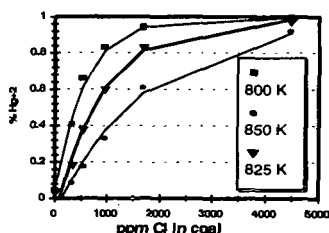


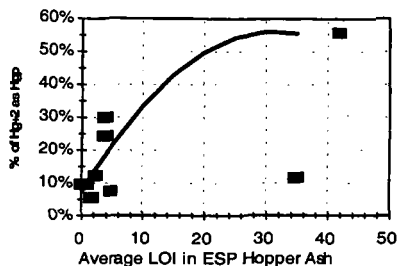
Figure 1. Predicted percentage of oxidized Mercury as a function of coal chlorine content.

Although, the oxidation of elemental mercury in the convective pass was assumed to proceed entirely via gas-phase reaction, experimental evidence suggests that some fly ash can catalyze oxidation of elemental mercury. Iron oxide is thought to be responsible for this oxidation.²⁸ Subsequent versions of the model may thus need to include a contribution from catalytic oxidation by fly ash. In this case, the iron content of the coal (and perhaps mineralogy) would be needed as input data.

At this time, it is not possible to generalize and conclude that high carbon in ash will always give high levels of particulate-bound mercury. However, in the case of similar coals, there may be a relationship as illustrated in Figure 2. The figure shows mercury measured in the ash, as sampled directly from the flue gas using the Ontario Hydro method, for nine different bituminous coals, all from the Northern Appalachian or Illinois Basins. The data were taken either at full scale power plants⁸ or at a large pilot scale unit.⁷ For these coals, there is a relationship between carbon content of ash (as measured by loss-on-ignition) and mercury content. However, the coals represented in the data are all very similar. Data will have to be obtained from a wider range of bituminous coals in order to generalize this relationship.

Western sub-bituminous coals produce fly ash which is very high in calcium. In some cases, ash from these coals has been observed to adsorb large amounts of mercury in the particulate collection device.¹⁰ Calcium silicate sorbents also adsorb mercury chloride.¹¹ However, western coals are generally low in chlorine and produce very little mercury chloride. Some

component of the ash from these coals appears to adsorb elemental mercury. At this time, the mechanism by which elemental mercury is removed by the ash from western sub-bituminous ash is not known.



The majority of utility plants use an electrostatic precipitator (ESP) for particulate control; approximately 10 per cent use a fabric filter or baghouse instead. In the laboratory, fly ash has been observed to act as a catalyst for oxidation of elemental mercury.¹² In other laboratory work,¹³ oxidized mercury has been observed to desorb from carbon-based sorbents and this may also occur for mercury adsorbed on fly ash in particulate control devices.^{7,9}

Figure 2. Mercury content of ash sampled at ESP inlet as a function of loss-on-ignition (LOI) of ESP hopper ash for nine different bituminous coals (References 7 and 8)

Much of the discussion of adsorption of mercury by ash in the convective section applies to the behavior of mercury in the particulate control device. Unfortunately, little recent data on the removal of mercury species across ESPs and baghouses exist. (Older data taken with EPA Method 29 have been shown to speciate mercury incorrectly.) In a pilot scale study conducted by McDermott Technologies and involving combustion of three different Ohio bituminous coals,⁷ gas-phase elemental mercury was removed by both a baghouse and an ESP, while oxidized mercury increased across both devices. This was also observed in a full scale power plant burning a North Dakota lignite.⁹ As mentioned previously, ash from certain western sub-bituminous coals has been shown to remove elemental mercury from flue gas, particularly at lower temperatures.¹⁴ Higher amounts of removal have been observed in baghouses relative to ESPs.

Since there are not enough data on the removal of mercury species across particulate control devices, no correlations have been developed for the preliminary model. Once a larger set of data has been assembled, it may be possible to derive relationships that take into account temperature, coal type, and particulate control device type.

A portion of the mercury may be adsorbed on the fly ash at the inlet to the particulate control device.^{7,12} Combustion of bituminous coals can result in unburned carbon which has been suggested to adsorb mercury. Mercury has been found to concentrate in the carbon-rich fraction of fly ash.¹⁵ Preliminary experimental work on adsorption of gaseous mercury on coal char¹⁶ showed that HgCl_2 was adsorbed more efficiently than Hg^0 , with two to fifty times more HgCl_2 adsorbed than Hg^0 under the same conditions, and the adsorption of the former was correlated with char surface area. This would also indicate that adsorption of HgCl_2 is a physical adsorption process. Adsorption of elemental mercury depended on the rank of the coal from which the char was derived. These results suggest that the nature of the unburned carbon, in terms of morphology and surface chemistry, strongly affects mercury adsorption.

Recent sampling campaigns on full scale utility boilers^{8,9} and a large pilot scale unit⁷ have provided data on the speciation of mercury before and after the FGD. Scrubbers have been observed to efficiently remove oxidized mercury, but not elemental mercury. Based on a detailed study of the behavior of mercury in a pilot scale wet scrubber,⁷ the adsorption of oxidized mercury appears to be strongly correlated with the mass transfer in the scrubber. The liquid-to-gas ratio (L/G) was a good indicator for the amount of Hg^{+2} removed by the scrubber. The composition of the scrubber liquid and design of the scrubber are also important in determining the removal of Hg^{+2} and the nature of the scrubbing solution must be known in order to model mercury removal.

Pilot scale data have been taken on the effect of scrubber slurry pH on mercury removal in limestone scrubbers.⁷ These suggest that the type of scrubber and the L/G ratio, not the pH, are the two key variables for modeling adsorption of Hg^{+2} across FGDs. Under some conditions, limestone scrubbers have been observed to reduce adsorbed mercury back to Hg^0 giving rise to higher concentrations of elemental mercury at the outlet than at the inlet. Assuming that no Hg^0

is adsorbed by the scrubber, the amount of adsorbed Hg^{+2} that is reduced can be calculated from the ratio of the increase in elemental mercury to the decrease in Hg^{+2} across the scrubber. Based on very limited data, this also appears to be related to the L/G ratio in the scrubber, although the effect is slight.

Figures 3 and 4 show a comparison of the measured and calculated values for mercury speciation (denoted by the fraction of mercury as Hg^{+2}) and total mercury emissions from the stack, respectively. The model predicts the stack emissions very well ($r^2=0.94$). Although the model is simple in its current form, it also predicts speciation well ($r^2 = 0.59$) using only limited information about the coal composition and operation of the air pollution control equipment. The model is able to predict a range of speciation from less than 5% Hg^{+2} to more than 30% Hg^{+2} .

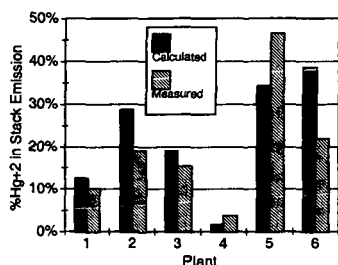


Figure 3. Predicted vs. measured stack speciation.

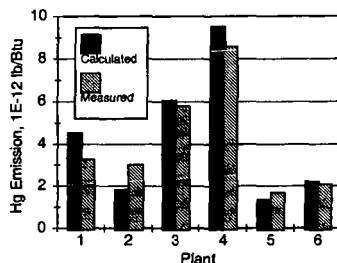


Figure 4. Predicted vs. measured emissions of mercury.

REFERENCES

1. Keating, M.H., et al. *Mercury Study Report to Congress, Volume I: Executive Summary*, EPA-452/R-97-003, December 1997.
2. Stein, E.D., Cohen, Y., and Winer, A.M. *Critical Rev. Environ. Sci. Technol.*, **1996**, 26, 1-43.
3. Pai, P., Karamchandani, P., and Seigneur, C. "Uncertainties in Modeling Long-Range Transport and Fate of Mercury Emissions in North America," presented at EPRI Managing Hazardous Air Pollutants, Fourth International Conference, Washington, DC, November 12-14, 1997.
4. Meij, R. (1994), *Fuel Processing Technology* 39: 199-217.
5. Prestbo, E.M. and Bloom, N.S. *Water, Air, Soil Poll.*, **1995**, 80, 145-158.
6. Fahlke, J. And Bursik, A. *Water, Air, Soil Poll.* **1995**, 80, 209-215.
7. Holmes, M.J., Redinger, K.E., Evans, A.P., and Nolan, P.S., "Control of Mercury in Conventional Flue Gas Emissions Control Systems," presented at the Fourth International Conference on Managing Hazardous Air Pollutants, Washington, D.C., November 12-14, 1997.
8. DeVito, M.S and Rosenhoover, W.A., "Flue Gas Mercury and Speciation Studies at Coal-Fired Utilities Equipped with Wet Scrubbers," presented at 15th International Pittsburgh Coal Conference, Pittsburgh, PA, September 15-17, 1998.
9. Laudal, D.L., "Mercury Speciation Sampling at Cooperative and United Power Associations' Coal Creek Station," Final Report, Energy & Environmental Research Center, University of North Dakota, January 1999.
10. Senior, C.L., Sarofim, A.F., Taofang, Z., Helble, J.J., and R.Mamani-Paco, *Fuel Processing Technology*, , **63**, 197-214 (2000).
11. Ghorishi, S.B. and Sedman, C.B., " *J. Air Waste Management Assoc.* **48**, 1191-1198 (1998).

12. Ghorishi, S.B., "Fundamentals of Mercury Speciation and Control in Coal-Fired Boilers," EPA-600/R-98-014, February 1998.
13. Miller, S.J., Dunham, G.E., Brown, T.D., and Olson, E.S., "Controlling Mechanisms That Determine Mercury Sorbent Effectiveness," presented at the Air & Waste Management Association 92nd Annual Meeting, St. Louis, Missouri, June 21-24, 1999, paper 99-898.
14. Sjostrom, S., Smith, J., Hunt, T., Chang, R., and Brown, T.D., "Demonstration of Dry Carbon-Based Sorbent Injection for Mercury Control in Utility ESPs and Baghouses," presented at the Air & Waste Management Association 90th Annual Meeting, Toronto, Ontario, Canada, June 8-13, 1997, paper 97-WA72A.07.
15. Li, Z. and Hwang, J.-Y., "Mercury Distribution in Fly Ash Components," presented at the Air & Waste Management Association 90th Annual Meeting, Toronto, Ontario, Canada, June 8-13, 1997, paper WP72B.05.
16. Wu, B., Peterson, T.W., Shadman, F., Senior, C.L., Morency, J.R., Huggins, F.E., and Huffman, G.P., " *Fuel. Proc. Technol.*, **63**, 93-108 (2000).

ATMOSPHERIC TRANSPORT, TRANSFORMATION, AND DEPOSITION OF MERCURY IN THE NORTHEASTERN UNITED STATES

Xiaohong Xu, Xiusheng Yang, David R. Miller, Joseph J. Helble, Robert J. Carley,
and Hugo Thomas
University of Connecticut
Storrs, CT 06269-4087

KEYWORDS: mercury deposition, mercury transport.

INTRODUCTION

The health risks associated with consumption of mercury contaminated fish are a widespread concern. It is generally believed that the atmospheric deposition of mercury is a major source of the observed elevated concentrations of mercury in fish. Atmospheric deposition is therefore directly related to mercury-based health concerns, but is a problem that cannot be addressed locally. Because of the complexity of the Hg cycle that involves the atmosphere, geosphere, and biosphere, Hg must be viewed in either a regional or global scale. This is particularly important due to its long atmospheric lifetime and ability to re-enter the atmosphere. In this study, methods described in Xu (1998) and Xu et al. (1999) were used to estimate the atmosphere-surface exchange of elemental Hg including emission and dry deposition. In this model, atmospheric transport and transformation of mercury were incorporated into a three-dimensional Eulerian air quality model that included soot and ozone and was fully coupled to in-cloud processes. The model was used to predict Hg concentration and deposition in the northeastern United States for one summer and one winter week during 1997. Additional simulations were also conducted to study the sensitivity of regional Hg deposition to the partitioning of Hg(II) between particulate and non-particulate forms.

MODEL DEVELOPMENT

The atmospheric transport and transformations of mercury were incorporated into SAQM (Sarmap Air Quality Model, Chang et al. 1987; 1996), a three-dimensional regional scale air quality model. A one-dimensional cloud module based on Chang et al. (1987), Dennis et al. (1993) and Tsai (1996) was incorporated into SAQM. Three mercury species were considered: elemental [Hg(0)], divalent [Hg(II)], and particulate [Hg(p)]. Soot particles were also considered. The major aqueous chemical processes included oxidation of dissolved Hg(0) by ozone, reduction of Hg(II) by sulfite, and adsorption of Hg(II) onto soot particles. The aqueous phase chemical reactions largely followed Petersen et al. (1995), but included three types of clouds: precipitating, co-existing non-precipitating, and fair weather clouds. The interaction between the in-cloud transformation of Hg(0) and direct scavenging of ambient Hg(II) was also considered. The air-surface exchange of Hg(0) was treated by explicitly considering both dry deposition and re-emission from bare soil, vegetation, and water surfaces (Xu et al., 1999).

Simulation periods and domain

Simulations were conducted for two weeks during the year 1997. The winter week simulation started at 1900 hours eastern standard time (EST) on Feb. 13 1997 and lasted 96 hours. For the summer week, the simulation started at 1900 EST on Aug. 20 1997 and lasted 120 hours. The domain of the simulation covered the northeastern U.S. and part of the Atlantic Ocean as shown in Fig. 1. Grid spacing considered 34×41 grids in the horizontal direction, with grid size of $12 \text{ km} \times 12 \text{ km}$, and 15 layers in the vertical direction with the center of the lowest layer located approximately 30 m above the ground. The top of the modeling domain was approximately 15.5 km. Meteorological data were taken from Pennsylvania State University (PSU), generated by the PSU/NCAR (National Center for Atmospheric Research) Mesoscale Model, Version 5 (MM5). The regional average precipitation predicted by MM5 was 4.67 cm and 1.94 cm for the summer and winter week, respectively.

Model input for the base case simulations

A baseline simulation was conducted using measured or estimated concentrations for the major pollutants. Hourly ozone concentrations were taken from near-surface measurements in the USEPA (United States Environmental Protection Agency) database with horizontal and vertical interpolation. Ambient soot concentrations were estimated from ozone and $\text{PM}_{2.5}$ measurements by the USEPA. Mercury emissions from combustion sources in Connecticut (CT) were provided by the Connecticut Department of Environmental Protection (CTDEP). Anthropogenic Hg emissions from other parts of the modeling domain were based on the USEPA study (USEPA, 1996). Speciation of Hg from combustion sources followed Petersen et al. (1995). Mercury

initial and boundary concentrations were set at 1.3 ng/m^3 for $\text{Hg}(0)$, and 0.01 ng/m^3 for each of $\text{Hg}(\text{II})$ and $\text{Hg}(\text{p})$.

Sensitivity simulations

Additional simulations were conducted by changing the speciation of Hg emission from anthropogenic sources or including adsorption of $\text{Hg}(\text{II})$ onto soot particles. The alternative emission speciation assumed all $\text{Hg}(\text{II})$ emissions were attached to particles. For the partitioning between ambient $\text{Hg}(\text{II})$ and $\text{Hg}(\text{p})$, an adsorption coefficient of $K = 3 \times 10^9 \times [\text{soot}]$ was adopted from Seigneur et al. (1998).

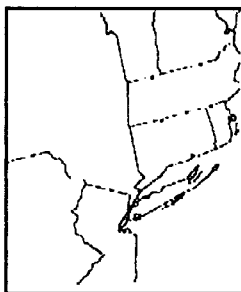


Figure 1. The domain of simulation.

Data analysis

For the baseline runs, the predicted weekly average ambient Hg concentrations and Hg concentrations in precipitation in CT were compared with weekly observations conducted by CTDEP and The University of Connecticut Environmental Research Institute (ERI). For comparing the sensitivity simulation results with those in the base case, the normalized deposition rates were calculated and presented by dividing the predicted regional daily average dry, wet, and total deposition with the corresponding value of the base case.

RESULTS AND DISCUSSION

Modeling results (base case) in comparison with monitoring data

Fig. 2 compares the model estimated summer week ambient concentrations of gaseous Hg [$\text{Hg}(0)+\text{Hg}(\text{II})$] and $\text{Hg}(\text{p})$ with measured values at eight monitoring stations in CT during the same time period. For gaseous Hg, the model was able to recapture the spatial variation as observed by the monitoring stations. The modeled values agreed well with monitoring data except at site WB where the measured Hg concentration was higher than at all other sites, for that week and throughout the year of 1997 (ERI, 1998). There are two possible reasons for the underprediction by the model at WB: the exclusion of several undocumented Hg emission sources in the emission inventory, or the location of the monitoring site too close to these or other local Hg sources.

The model overpredicted the ambient $\text{Hg}(\text{p})$ concentration at all eight monitoring sites (Fig. 2b). The modeled values were also higher than $\text{Hg}(\text{p})$ concentrations measured in other regions, which ranged from 0.011 ng/m^3 in Underhill Center, VT (Burke et al., 1995) to 0.094 ng/m^3 in Detroit, MI (Keeler et al., 1995). This might have reflected the limitation of the model in handling the broad distribution of particle sizes. Because the largest particles will be poorly mixed and will deposit close to the stack, it is likely that the model would underestimate dry deposition and hence overestimate ambient concentrations of $\text{Hg}(\text{p})$.

The predicted summer week precipitation results agreed reasonable well with measurements (Fig. 3a). The modeled total Hg concentrations in precipitation, ranging from 7.68 to 11.7 ng/l , were higher than observations in general, as shown in Fig. 3b. The model estimates were comparable with published measurements (e.g. Fitzgerald et al., 1991; Rea et al., 1996; Keeler and Hoyer, 1997).

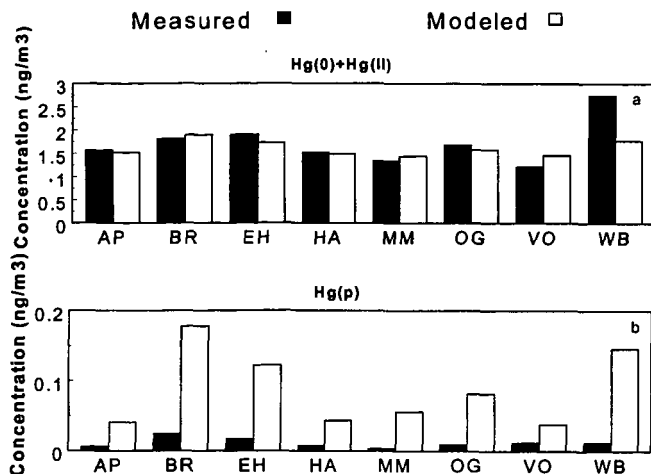


Figure 2. Comparison of modeled gaseous Hg concentrations (a) and Hg(p) concentrations (b) with monitored values in CT stations, during the summer week simulation. AP-Avery Point, BR-Bridgeport, EH-East Hartford, HA-Hammonasset, MM-Mohawk Mountain, OG-Old Greenwich, VO-Voluntown, WB-Waterbury.

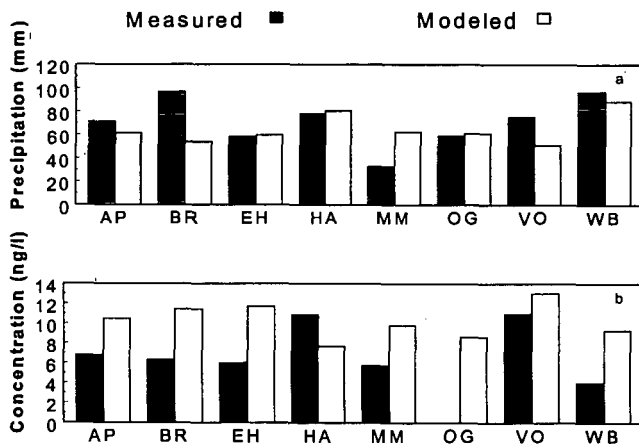


Figure 3. Comparison of modeled weekly precipitation (a) and Hg concentrations in precipitation (b) with monitored values in CT stations, during the summer week simulation. Concentration measurement was not available at OG.

The comparison between winter week simulation and measurements was similar to that of the summer week, with good agreement in gaseous concentration and precipitation concentration, but overprediction of ambient Hg(p) concentration.

Effects of emission speciation and Hg(II) adsorption to soot on Hg deposition

Table 1 lists normalized wet, dry, and total deposition of the region for the summer and winter week. By assuming all Hg(II) emissions were attached to particles, the ambient concentrations of Hg(p) increased, and concentrations of Hg(II) decreased. There was a significant decrease in dry deposition of Hg(II), but a large increase in the dry deposition of Hg(p). The total dry deposition decreased dramatically. This is because the dry deposition velocity of Hg(p) was much lower than that of Hg(II). The total wet deposition increased over the base case, as reported by Bullock et al. (1997), primarily due to a significant increase in wet deposition of Hg(p) and Hg(0). The resulting total deposition was less than in the base case.

When Hg(II) adsorption to soot particles was considered, the resulting partitioning between ambient Hg(II) and Hg(p) caused a decrease in the dry deposition of Hg(II) and an increase in the dry deposition of Hg(p), but to a lesser extent than in the case of alternative emission speciation. Similarly, the gas phase partitioning led to less wet deposition of Hg(II), and more wet deposition of Hg(p) and Hg(0). Compared with the alternative emission speciation, the Hg(II) adsorption to particles resulted in less reduction of total deposition because the alternative emission speciation influenced heavily concentrations near the surface where point sources were located. Thus, Hg(II) dry deposition was largely reduced, leading to much lower dry deposition.

As can be seen from Table 1, deposition during the winter was more sensitive to changes in ambient Hg(II) concentration compared with the summer week. This can be largely attributed to the different Hg species that predominate the deposition during warm and cold seasons. In the winter week, approximately 65% of total deposition was from Hg(II), in comparison with 40% in the summer week.

Table 1. Normalized regional deposition from model simulation during the summer and winter weeks.

| Simulation | Summer | | | Winter | | |
|---|----------|----------|-------|----------|----------|-------|
| | Dry dep. | Wet dep. | Total | Dry dep. | Wet dep. | Total |
| Alternative emission speciation | 0.57 | 1.14 | 0.76 | 0.27 | 1.19 | 0.52 |
| Adsorption of Hg(II) to soot, gas phase | 0.78 | 1.10 | 0.89 | 0.48 | 1.16 | 0.67 |

SUMMARY AND CONCLUSIONS

Model predictions of surface level gaseous Hg concentrations were close to measured levels, agreeing to within 12% on average, about half the estimated error in measurements. The predicted Hg concentrations in precipitation were 50% higher than measured values on average, slight lower than the estimated 60% error in measurements. The modeled ambient particulate Hg concentrations, on the other hand, were much higher than measurements made in CT and other places, suggesting an underestimation of dry deposition in the source grids.

Both the alternative emission speciation and the adsorption of ambient Hg(II) onto soot particles resulted in less total deposition of Hg, indicating the dependence of total deposition on the fraction of gaseous mercury bound to particles. It is therefore important to determine accurately the emission speciation and transformation during transport.

In conclusion, the model was shown to be capable of producing acceptable results, and useful in analyzing the effects of various environmental factors on the atmospheric transport, transformation, and deposition of Hg. More simulations to address seasonal variations and to further evaluate the model are being conducted.

ACKNOWLEDGMENTS

This study was jointly supported by the Connecticut Department of Environmental Protection, the University of Connecticut Environmental Research Institute, and The Research Foundation of the University of Connecticut. The authors would like to thank Dr. Julius S. Chang at State University of New York at Albany, for providing SAQM and advising its modification, and Dr. Nelson L. Seaman and Mr. Glenn Hunter at the Pennsylvania State University for providing the meteorology data.

REFERENCES

- Bullock Jr. O. R., Benjey W. G. and Keating M. H, 1997: The modeling of regional-scale atmospheric mercury transport and deposition using RELMAP. pp 323-347. In *Atmospheric Deposition of Contaminants to the Great Lakes and Coastal Waters*. Ed. J. E. Baker. SETAC Press. Pensacola, Florida.
- Burke, J., M. Hoyer, G. Keeler, and T. Scherbatskoy, 1995: Wet deposition of mercury and ambient mercury concentration at site in the Lake Champlain basin. *Water, Air, and Soil Pollution*. 80, 353-362.
- Chang, J. S., R. A. Brost, I. S. A. Isaksen, S. Madronich, P. Middleton, W. R. Stockwell, and C. J. Walcek, 1987: A three-dimensional Eulerian acid deposition model: physical concepts and formation. *Journal of Geophysical Research*. 92(D12), 14681-14700.

- Chang, S. J., Y. Li, M. Beauharnois, H. Huang, C. Lu, and G. Wojcik, 1996: *SARMAP Air Quality Model*. Atmospheric Science Research Center, University at Albany, State University of New York, 100 Fuller Road, Albany, New York 12205.
- Dennis, R. L., J. N. McHenry, W. R. Barchet, F. S. Binkowski, and D. W. Byun, 1993: Correcting RADM's surface underprediction: discovery and corrections of model errors and testing the corrections through comparisons against field data. *Atmospheric Environment*. 27A(60), 975-997.
- ERI, 1998: *Annual Progress Report of Connecticut Atmospheric Mercury Monitoring Network*. Environmental Research Institute, The University of Connecticut. Storrs, Connecticut.
- Fitzgerald, W. F., R. P. Mason, and G. M. Vandal, 1991: Atmospheric cycle and air-water exchange of mercury over mid-continental lacustrine regions. *Water, Air, and Soil Pollution*. 56, 745-767.
- Keeler, G., G. Glinsorn, and N. Pirrone, 1995: Particulate mercury in the atmosphere: its significance, transport, transformation and sources. *Water, Air, and Soil Pollution*. 80, 159-168.
- Keeler, G. J., and M. Hoyer, 1997: Recent measurements of atmospheric mercury in the Great Lakes region. pp305-321. In *Atmospheric Deposition of Contaminants to the Great Lakes and Coastal Waters*. Ed. J. E. Baker. SETAC Press. Pensacola, Florida.
- Northeast Regional Climate Center, 1997: *New England Climate*. 97(8). Ithaca, New York.
- Petersen, G., A. Iverfeldt, and J. Munthe, 1995: Atmospheric mercury species over central and northern Europe. Model calculations and comparison with observations from the Nordic Air and Precipitation Network for 1987 and 1988. *Atmospheric Environment*. 29(1), 47-67.
- Rea, A. W., G. J. Keeler, and T. Scherbatskoy, 1996: The deposition of mercury in throughfall and litterfall in the Lake Champlain watershed: a short term study. *Atmospheric Environment*. 30(19), 3257-3263.
- Seigneur C., Abeck H., Chia G., Reinhard M., Bloom N. S., Prestbo E., and Saxena P, 1998: Mercury adsorption to elemental carbon (soot) particles and atmospheric particulate matter. *Atmospheric Environment*. 32(14/15): 2649-2657.
- Tsai, Y., 1996: *Evaluation of two one-dimensional cloud models used in air quality models*. Thesis. Department of Atmospheric Science, University at Albany, State University of New York, 100 Fuller Road, Albany, New York 12205.
- USEPA, 1996: *Mercury study report to congress. Vol. II: An inventory of anthropogenic mercury emission in the United States*. Office of air quality Planning and Standards, Research Triangle park, NC, U.S.A.
- Xu, X., 1998: *A modeling study of regional scale atmospheric transport and transformation of mercury*. Ph.D. Dissertation. The University of Connecticut. Storrs, CT 06269.
- Xu X., Yang, X., Miller D. R., Helble J. J., and Carley R. J, 1999: Formulation of bi-directional air-surface exchange of elemental mercury. *Atmospheric Environment*. 33(27), 4345-4355.

STRUCTURE OF PRIMARY PM_{2.5} DERIVED FROM DIESEL TRUCK EXHAUST

G. P. Huffman, F. E. Huggins, N. Shah and S. Pattanaik
University of Kentucky, CFELS, 111 Whalen Building,
533 S. Limestone St., Lexington, KY 40506

H. L. C. Meuzelaar and Sun Joo Jeon,
Department of Chemical & Fuels Engineering,
University of Utah, Salt Lake City, UT

D. Smith and B. Harris
U.S. Environmental Protection Agency, National Risk Management Res. Lab.,
Research Triangle Park, NC 27711

M. S. Seehra and A. Manivannan,
Physics Department, West Virginia University, Morgantown, WV

Key-Words: Particulate matter, PM_{2.5}, Diesel engine exhaust, thermal desorption GC/MS, XAFS spectroscopy, SQUID magnetometry

INTRODUCTION

The U.S. Environmental Protection Agency is currently considering regulations on airborne particulate matter < 2.5 microns in mean diameter (PM_{2.5}). It is important that the molecular structure and microstructure of PM_{2.5} from various sources be thoroughly characterized in order to identify structural features that may be important for source apportionment and health effects. Two of the primary sources of PM_{2.5} from petroleum are combustion of residual fuel oil and diesel engines. In previous papers, we have discussed the structure of PM_{2.5} derived from the combustion of residual fuel oil.^(1,2) In the current paper, we report some preliminary results on the molecular structure of primary PM_{2.5} from diesel vehicle tests. The techniques employed included thermal desorption (TD) GC/MS, x-ray absorption fine structure (XAFS) spectroscopy, and SQUID magnetometry.

SAMPLE GENERATION AND COLLECTION

The sample generation experiments were conducted by Harris and Smith at the EPA National Risk Management Research Laboratory (NRMRL). The samples were collected on teflon and quartz filters from the exhaust stack of a heavy-duty diesel truck. The total distance traveled by the truck during the sampling run was 191 miles at an average speed of 60.4 MPH. Diesel exhaust gas was sampled via a heated probe located two feet below the top of the exhaust stack. Hot exhaust gas passed through a PM_{2.5} cyclone and was subsequently cooled and diluted with ambient air. The average total stack gas exhaust rate over the duration of the sampling period was 15.5 Lpm. Four samples were collected simultaneously by establishing different gas flow rates to each of four filters, each 48 mm in diameter. This yielded two heavily loaded quartz filters (B and C, 6.2 mg of PM), one lightly loaded quartz filter (D, .5 mg of PM), and one lightly loaded Teflon (PTFE) filter (A, .6 mg of PM). Two additional filters (labeled PM1 and PM2) with intermediate loading (~2mg) were collected in a separate experiment.

ANALYTICAL CHARACTERIZATION

Thermal desorption GC/MS methodology

Filter strips (1.5 x 18 mm²) are positioned inside a special glass reaction tube that is lined with a ferromagnetic foil with a Curie temperature of 315°C. The tube is placed into a Curie-point reactor for desorption of volatile (VOC) and semivolatile organic compounds (SVOC). In Curie-point desorption, a high frequency coil surrounds the glass tube and heats the foil by induction. The foil heats up till its Curie point is reached and its energy intake drops, thus holding the temperature of the foil at this point. Flash desorption of organic compounds from the particles immobilized by the filter strips is achieved using a total heating time of 10 s under a continuous flow of He carrier. The continuous flow of He transfers the analytes from the reaction zone into a fused silica capillary column of a gas chromatograph, coupled to a mass spectrometer. A more detailed description of the apparatus is given elsewhere.⁽³⁾

Conventional solvent-based extraction method has been used for extraction of soluble analytes from a more or less insoluble matrix. However, there are several practical problems with the application of solvent-based GC/MS techniques to ambient PM filter sample characterization,

compared to the TD method. Solvent-based GC/MS analysis of filter samples requires relatively large sample masses and the laboratory methods involved are laborious and use large quantities of solvents. Solvent extracts can include significant quantities of large soluble or even polymeric molecules that are unsuitable for direct GC/MS analysis but may contaminate the GC inlet.

The two heavily loaded quartz filters (B and C), produced qualitatively and quantitatively similar TD-GC/MS profiles. The data for sample B are shown in Figures 1 and 3. The TIC are marked by a strong *n*-butylbenzenesulfonamide peak, together with some of the ubiquitous alkylphthalate contaminants, notably dimethylphthalate. Hopanes and steranes are virtually absent.

Compared to the high flow samples B and C, the lightly loaded quartz fiber filter D produces approx. 40 % of the long chain alkane signal intensities and 25 % of the PAH intensities. Since the "total PM mass" of sample D should only be 10 % of samples B and C, there is an obvious nonlinear response within the five-step analytical procedure (i.e. sample collection + sample preservation during storage and transportation + filter subaliquotting + thermal desorption + GC/MS response).

The TIC of the lightly loaded Teflon (PTFE) filter sample A shows a drastic reduction in the first "hump", which represents an unresolved complex mixture, and an increase in the yield of the highly polar and labile *n*-alkanoic acids (Figure 2). Perhaps the most surprising finding is the strong even vs. odd predominance among the long chain alkanes (Figure 4). The opposite phenomenon (odd vs. even predominance) is well known among geochemical samples and is generally attributed to decarboxylation of biogenic fatty acids with even carbon numbers. A highly speculative interpretation could be that the even vs. odd *n*-alkane predominance shown by the PTFE filter desorbate is in fact the correct relative abundance for the particle-borne long chain alkanes, as is the even vs. odd *n*-alkanoic acid abundance. Both observations might be explained by synthetic, 2-carbon pathways in the soot formation process. During desorption of alkanolic acids from the quartz filter, however, a substantial amount of decarboxylation may occur, thereby turning the dominant, even carbon number, alkanolic acids in to odd carbon number *n*-alkanes, thereby smoothing out the dips in the *n*-alkane distribution profile.

XAFS spectroscopy analysis

XAFS spectra were obtained at the S K-edge at beam line X-19A at the National Synchrotron Light Source (NSLS) and at the Cr, Fe, Ni and Zn K-edges at beam line 4-3 at the Stanford Synchrotron Radiation Laboratory (SSRL) and at beam line X-18B at NSLS. The concentrations of Fe and Zn (800 - 2000 ppm) were significantly higher than those of other metals in the samples and gave correspondingly better quality spectra. All spectra were collected in the fluorescent mode, using a Lytle detector for the sulfur spectra and a 13 element solid-state Ge detector for the metal spectra. Experimental procedures are described in detail elsewhere.^(4,5)

Figure 5 shows a typical S K-edge XANES spectrum, deconvoluted into its component peaks. The locations of the peaks are used to assign each feature to a particular molecular form of valence state of sulfur, as indicated by the labels in Figure 5. Then, using previously developed methodology,⁽⁴⁾ the areas under the various peaks can be converted into percentages of the total sulfur contained in each of the molecular forms or valence states identified. The results of this analysis for the diesel PM_{2.5} samples are summarized in Table 1. It is seen that sulfate is the dominant sulfur form, followed by a sulfone species (most probably the *n*-butylbenzene sulfonamide identified by TD/GC/MS), and a small amount of thiophenic sulfur.

Although the XAFS spectra of the metals were quite noisy given the small amount of material under irradiation, useful XANES spectra were obtained from iron and zinc. Whereas the iron XANES spectra appeared to be similar to ferric sulfate, the zinc XANES spectra were quite different from that of zinc sulfate. Chromium sulfate was identified in sample C2.

SQUID magnetometry

A SQUID magnetometer (Quantum Design Model MPMS) was used to measure the temperature variation of the magnetization, *M*, from 5 K to 350 K of several of the diesel PM_{2.5} samples. The data are corrected for the diamagnetic contribution (measured in separate experiments) from the filter and the polyethylene sample holder.

The variations observed for the samples PM1 and PM2 are nearly identical, both in magnitude as well as in temperature variation. In these cases, there is a rapid increase in *M* below 25 K, above which *M* is nearly temperature independent. For sample B, the rise in *M* at lower temperatures is spread over a larger temperature range, whereas for sample C, *M* is nearly temperature independent, with only a hint of an increase below 10 K.

The increase in M at lower temperatures can be described by the Curie-law $M = M_0 + CH/T$ where $C = N\mu^2/3k_B$ is the Curie constant, N is the concentration of impurities each with magnetic moment μ , and k_B is the Boltzmann constant.⁽⁶⁾ The plots of $(M - M_0)$ versus $1/T$ are linear below ~ 25 K for samples PM2, PM1 and B. Using $\mu = 1.7 \mu_B$ for spin $S = 1/2$ yields $N = 10, 5$ and 2 (in units of $10^{19}/g$) for PM2, PM1 and B, respectively. These levels of impurities have been observed from similar analysis in high purity activated carbon.⁽⁷⁾ The nature of these impurities including free radicals by low temperature electron spin resonance spectroscopy in the near future.

Acknowledgement: Support of this research under U.S. Department of Energy (FE/NPTO) contract No. DE-AC26-99BC15220 is gratefully acknowledged. The XAFS experiments were conducted at the Stanford Synchrotron Radiation Laboratory and the National Synchrotron Light Source, which are also supported by the U.S. DOE.

REFERENCES

1. G. P. Huffman, F. E. Huggins, N. Shah, R. Huggins, W. P. Linak, C. A. Miller, R. J. Pugmire, and H. L. C. Meuzelaar, *ACS Div. Fuel Chem. Preprints*, **45**(1), 6-10 (2000).
2. G. P. Huffman, F. E. Huggins, N. Shah, R. Huggins, W. P. Linak, C. A. Miller, R. J. Pugmire, H. L. C. Meuzelaar, M. Seehra, and A. Mannivannan, "Characterization of Fine Particulate Matter Produced by Combustion of Residual Fuel Oil," *J. Air & Waste Management Assoc.*, **50**, (2000), in the press.
3. Dworzanski, J.P.; McClennen, W.H.; Cole, P.A.; Thornton, S. N.; Arnold, N.S.; Snyder, A.P.; Meuzelaar, H.L.C., *Environ. Sci. Technol.*, **31**, 295-305 (1997).
4. G.P. Huffman, S. Mitra, F.E. Huggins, N. Shah, S.Vaidya, and F. Lu, *Energy & Fuels*, **5**, 574-581 (1991).
5. F.E. Huggins, N. Shah, J. Zhao, F. Lu, and G.P. Huffman, *Energy & Fuels*, **7**, 482-489 (1993).
6. V. S. Babu, L. Farinash and M. S. Seehra, *J. Mater. Res.*, **10**, 1075 (1995).
7. A. Manivannan, M. Chirila, N. C. Giles and M. S. Seehra, *Carbon*, **37**, 1741 (1999).

Table 1: Sulfur forms in diesel PM samples

| Sample | Elemental S | Thiophene | Sulfone* | Sulfate |
|-------------------|-------------|-----------|----------|---------|
| Diesel Filter PM1 | < 1 | 3 | 7 | 90 |
| Diesel Filter PM2 | < 1 | 6 | 8 | 86 |
| Diesel B2 9/99 | < 1 | < 1 | 2 | 98 |
| Diesel C2 9/99 | < 1 | 5 | 11 | 84 |

*Probably n-butylbenzenesulfonamide contaminant (see text)

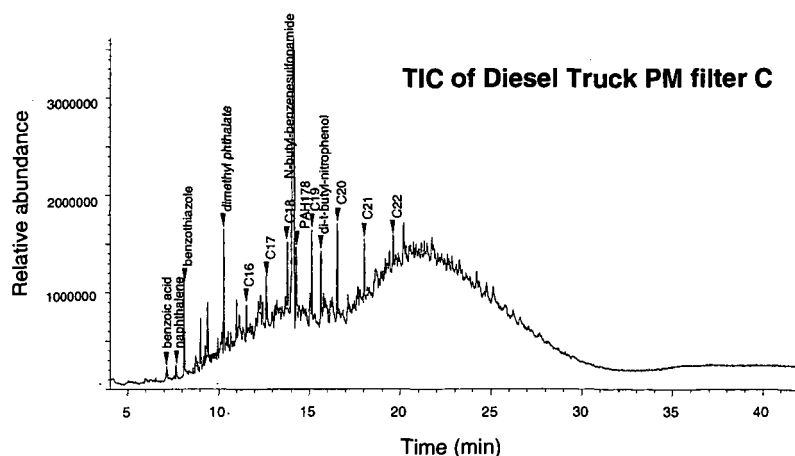


Figure 1: TIC of a heavily loaded diesel exhaust PM_{2.5} filter.

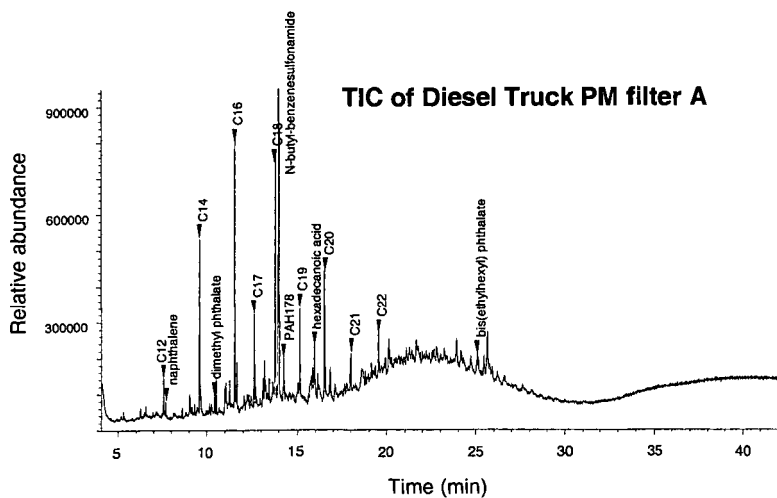


Figure 2. TIC of a lightly loaded diesel exhaust PM_{2.5} filter.

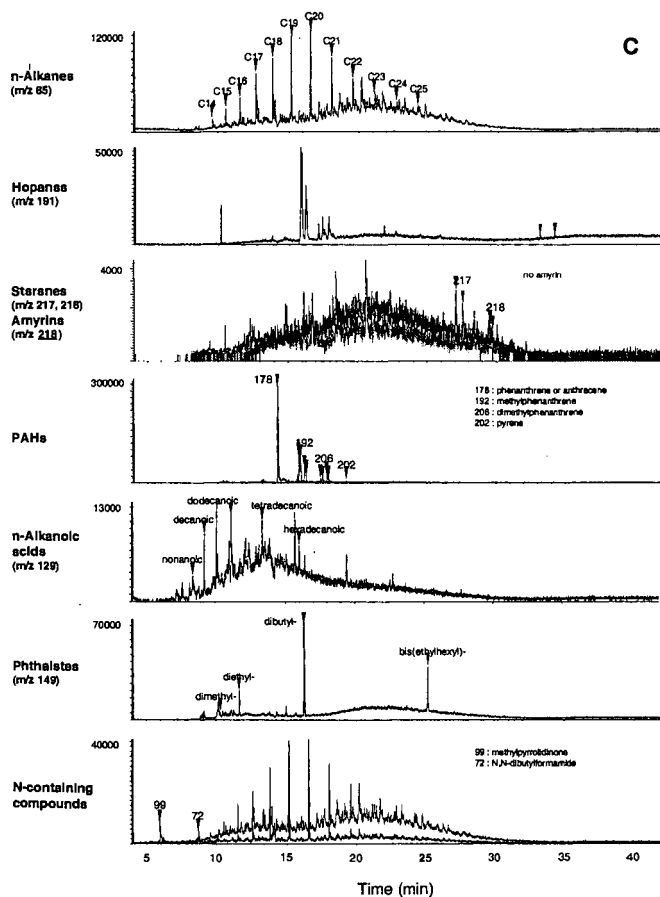


Figure 3: MS data for heavily loaded diesel exhaust PM_{2.5} filter sample B

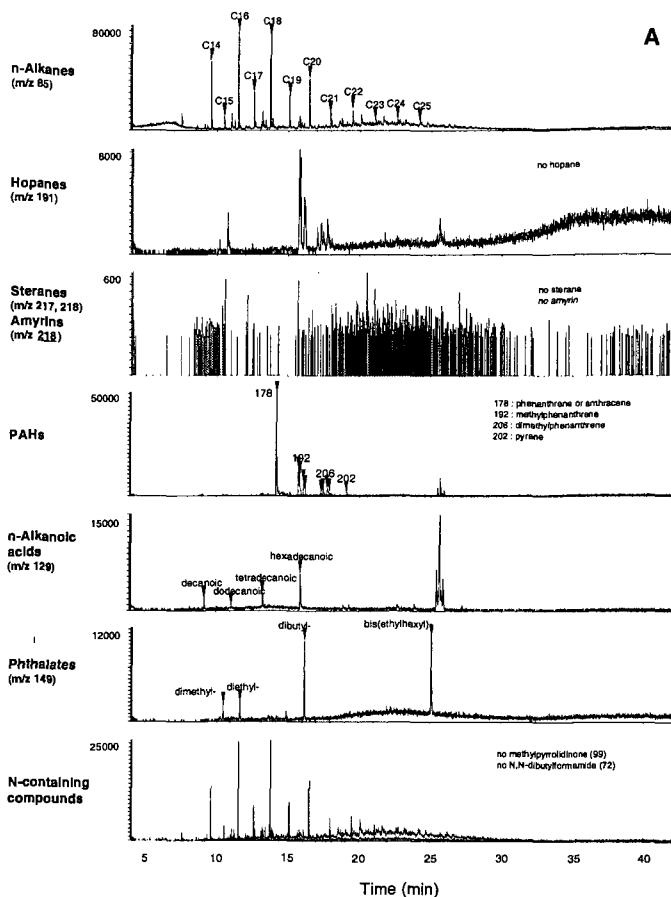


Figure 4. MS data for lightly loaded diesel exhaust PM_{2.5} filter sample.

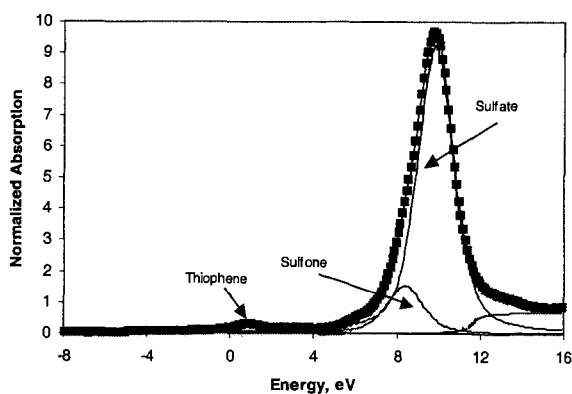


Figure 5: Least-squares fitted Sulfur K-edge XANES spectrum of Diesel PM sample "C2". The sulfone component is probably due to the n-butylbenzenesulfonamide contamination (see test).

IDENTIFICATION OF INORGANICS IN THE NIST SRM1648 SAMPLE OF URBAN PARTICULATE MATTER

A. Manivannan and M. S. Seehra
Physics Department, West Virginia University,
PO Box: 6315, Morgantown, WV 26506-6315

KEYWORDS: Particulate Matter, X-ray Diffraction, Electron Spin Resonance, Magnetometry

ABSTRACT

X-ray diffraction, electron spin resonance (ESR) and magnetometry studies are reported on the urban particulate matter sample NIST1648. This is a time-integrated sample of urban particulate matter collected over 12 months in St. Louis. We have identified major chemical compounds present in this sample. In XRD, the sharp lines match the spectra of the following crystalline compounds: gypsum ($\text{CaSO}_4 \cdot 2\text{H}_2\text{O}$), quartz (SiO_2), illite (K-Al-Si-O-OH), kaolinite (Al-Si-O-OH), zinc sulfite hydrate ($\text{ZnSO}_3 \cdot 2\text{H}_2\text{O}$), zinc sulfate sulfite hydrate ($\text{Zn}_2(\text{SO}_3)(\text{SO}_4) \cdot 3\text{H}_2\text{O}$), zinc arsenate hydrate ($\text{Zn}_3(\text{AsO}_4)_2 \cdot 4\text{H}_2\text{O}$), and iron sulfate ($\text{Fe}_2(\text{SO}_4)_3$). Magnetometry measurements indicate the presence of Mn_2O_3 , Fe_3O_4 and $\alpha\text{-Fe}_2\text{O}_3$. In ESR spectroscopy, lines due to Fe_3O_4 and Fe^{2+} have been identified.

INTRODUCTION

Air-borne ambient particulate matter (PM) is a mixture of particles directly emitted into the air from fossil fuel combustion such as coal, oil, electrical power plants and automobile exhausts. According to the US Environmental Protection Agency (EPA), particulate matter less than 10 microns in diameter (PM_{10}) and more recently less than 2.5 microns (fine PM or $\text{PM}_{2.5}$) is of particular concern [1]. The implementation of this new rule requires the acquisition of important scientific information regarding the effects of $\text{PM}_{2.5}$ on public health and welfare. These adverse health effects include premature mortality, aggravation of respiratory and cardiovascular symptoms, change in lung structure, and altered respiratory defense mechanisms [2-4]. Two controversial studies (the Harvard University six-city study and the American Cancer Society study) have linked the presence of fine particulate matter to premature mortality [5]. Generally, fine particles are considered to be more hazardous than coarse particles. Therefore, the analysis have to be done at molecular levels. In order to understand the molecular speciation and its parameters such as valency, solubility, acidity, and composition, it is essential to identify and analyze the elements and compounds present accurately by employing several analytical tools. Huggins et al., [6] have carried out x-ray absorption fine structure (XAFS) and proton induced x-ray emission (PIXE) analysis to investigate several elements in the SRM1648 urban particulate matter sample supplied by NIST (National Institute of Standards and Technology). The emphasis is placed on those elements that are either transition metals or elements defined as hazardous air pollutants in the 1990 Amendments to Clean Air Act [7].

In this paper, we present results of our investigations on the determination of the chemical compounds in the NIST standard reference material SRM1648. This sample is used as the control material in the evaluation methods used in the analysis of atmospheric particulate matter and materials with similar matrix. One of the main focus in the present work is to identify the chemical formulae of the compounds present in PM. Information on the nature of chemical compounds present in this material is essential in understanding the chemical pathways that leads to their formation. We have employed x-ray diffraction (XRD), magnetometry and electron spin resonance (ESR) spectroscopy to identify the various components present in SRM1648. Details of these results and their discussion are presented below.

EXPERIMENTAL

The sample SRM1648 of urban PM [8] was obtained from NIST. It was collected in St Louis, MO area over a 12-month period in a bag-house designed especially for the purpose. The collected particulate material was removed from the filter bags, combined into a single lot, screened through a fine-mesh sieve to remove extraneous materials and thoroughly blended in a V-blender and then packed into bottles [8].

The PIXE (proton-induced X-ray emission) spectroscopy of this sample reported by Huggins et al [6] showed the presence of Al (2.33%), Si (7.92%), S (4.55%), Ca (5.52%), Fe (3.29%) and

the elements (C,H,O,N) = 70%. Other elements present in ppm levels (shown in parenthesis) are Na (5000), Mg (5300), P (7700), Cl (4000), K (8300), Ti (3500), Zn (4130) and Pb (6720), with even smaller amounts of Cr, Mn, Ni, Cu, Br, and Sr.

The X-ray analysis was performed using a Wide Angle X-ray Diffractometer (WAXD) from Rigaku (Model D/MAX) using Cu K α radiation with $\lambda = 1.542 \text{ \AA}$. The other experimental conditions include $\frac{1}{2}$ degree divergence and scatter slits, 0.15mm receiving slits, step scans with 0.04 degree steps and 30sec counting time at each step, and intensity measured in counts. This relatively slow scan process enabled us to obtain the diffraction pattern with resolved sharp lines due to various compounds. The analysis of the x-ray patterns was carried out using Jade software package supplied by MDI (Materials Data Inc.) and the JCPDS data files. Magnetization measurements were done in the 5K to 350K range using a SQUID magnetometer (Quantum Design Model MPMS). ESR spectroscopy of the sample was carried out using a standard reflection type X-band spectrometer.

RESULTS AND DISCUSSION

In Figure 1 we show the x-ray diffraction pattern of the NIST SRM1648 sample. In this pattern, sharp lines due to crystalline components are superposed on a broad peak centered around $2\theta = 25^\circ$. This broad peak around 25° is characteristics of amorphous carbon [10]. Using the search/match program of the Jade software together with the help of JCPDS data base, we have identified almost all the observed crystalline peaks shown in Fig. 1. They are due to gypsum ($\text{CaSO}_4 \cdot 2\text{H}_2\text{O}$), quartz (SiO_2), kaolinite (Al-Si-O-OH), illite (K-Al-Si-O-OH), zinc arsenate hydrate ($\text{Zn}_3(\text{AsO}_4)_2 \cdot 4\text{H}_2\text{O}$), zinc sulfite hydrate ($\text{ZnSO}_3 \cdot 2\text{H}_2\text{O}$), zinc sulfate sulfite hydrate ($\text{Zn}_2(\text{SO}_3)(\text{SO}_4) \cdot 3\text{H}_2\text{O}$), and iron sulfate ($\text{Fe}_2(\text{SO}_4)_3$). The major contribution of the present investigation using x-ray diffraction is that we are able to identify various compounds and their water content in this sample. In making the identifications, we compared the diffraction patterns of all appropriate compounds available in the JCPDS files. The concentrations of the elements Al (2.33%), Si (7.92%), S (4.55%), Ca (5.52%), and Fe (3.29%) can be explained by the strong crystalline peaks in x-ray diffraction for their respective compounds mentioned above. In addition to the elemental data reported by Huggins et al. [6], x-ray diffraction analysis identifies the possible compounds present in the sample as a complimentary study. One important observation is the presence of gypsum ($\text{CaSO}_4 \cdot 2\text{H}_2\text{O}$) which is not reported in the NIST certificate of analysis. All of the compound reported here can affect human health. Quartz and the arsenic compounds may be specially hazardous [11].

Since the sensitivity of WAXD for detecting elements and compounds in a mixture is at best limited to individual concentrations of 1% or more, we have employed magnetometry and ESR spectroscopy for possible detection of other materials. In Fig. 2, temperature variation of the magnetization of the sample SRM 1648 is shown. The arrows indicate the positions where magnetic transitions due to Mn_3O_4 ($T_c = 43 \text{ K}$ [12]), Fe_3O_4 ($T_c = 120 \text{ K}$) and $\alpha\text{-Fe}_2\text{O}_3$ ($T_c = 260 \text{ K}$) are known [13]. In order to confirm these assignments, a laboratory prepared mixture of Fe_3O_4 , Mn_3O_4 and $\alpha\text{-Fe}_2\text{O}_3$ in 1:1:1 ratio by weight was investigated (Fig. 2) by magnetometry. The transition temperatures observed in SRM1648 match with the three oxides, confirming our identifications. The concentration of Mn_3O_4 is relatively small in SRM1648 as indicated by the weakness of the peak near 43K. The results obtained by magnetometry provide evidence for the usefulness of this technique for detecting ferrimagnetic and ferromagnetic materials in quantities too small to be detected by x-ray diffraction.

The ESR spectroscopy of SRM1648 carried out room temperature and at 9.2GHz shows several lines (Fig.3). The main line with $g = 2.2$ and linewidth $\Delta H = 688 \text{ G}$ is probably due to Fe_3O_4 . The line at $g = 3.57$ (Fig.4) matches the location expected for Fe^{2+} species in octahedral symmetry [14]. The remaining lines are clearly a part of the hyperfine structure. However because of lack of resolution, we are not able to identify all the lines and hence their origin at this time remains unresolved. Perhaps, with variable temperature ESR spectroscopy, we might be able to resolve this issue in the near future.

In summary, with the combined use of WAXD, magnetometry and ESR spectroscopy, we have been able to identify a significant number of chemical compounds present in the NIST SRM1648 sample of urban particulate matter. This information combined with the data available from PIXE and XAFS on the elemental concentrations [6] provides a nearly complete analysis of the major constituents of this sample.

ACKNOWLEDGEMENT

Support of this research under the U.S. Department of Energy contract No. DE-AC26-99BC15220 is gratefully acknowledged. We thank Dr. G. P. Huffman and Dr. F. E. Huggins for useful consultations and for providing a copy of their paper [Ref.6] prior to publication.

REFERENCES

1. Federal Register, 62 FR 38652, July 18, 1997.
2. D. W. Dockery, C. A. Pope, X. Xu, J. D. Spengler, J. H. Ware, M. E. Fay, B. G. Ferris, and F. E. Speizer, *New England J. Med.*, 329 (1993) 1753.
3. R. T. Burnett, R. Dales, D. Krewski, R. Vincent, T. Dann, and J. R. Brook, *Am. J. Epidemiology*, 142 (1995) 15.
4. J. Schwartz, and R. Morris, *Am. J. Epidemiology*, 142 (1995) 23.
5. Chemical Engineering News, Particulate Matter Health Studies to be Reanalyzed August 18, (1997) 33.
6. F. E. Huggins, G. P. Huffman, and J. D. Robertson, *J. Haz. Mat.* (in press)
7. Amendments to Clean Air Act, U.S. Public Law 101-549, U.S. Gov. Printing Office, 1990, 314 pp.
8. National Institute of Standards & Technology, Certificate of Analysis, Standard Reference Material 1648, Urban Particulate Matter, August 30, 1991, 5 pp.
9. V. S. Babu, L. Farinash and M. S. Seehra, *J. Mater. Res.*, 10, 1075 (1995).
10. A. Manivannan, M. Chirila, N. C. Giles and M. S. Seehra, *Carbon* 37 (1999) 1741.
11. R.S. Pandurangi, M. S. Seehra, B. L. Razzaboni and P. Bolsaitis: *Environ. Health Perspectives*, 86 (1990) 327.
12. G. S. Chaddha, and M. S. Seehra, *J. Phys D: Appl. Phys.* 16 (1983) 1767.
13. G. Srinivasan and M. S. Seehra, *Phys. Rev. B* (1983) 1.
14. Paramagnetic Resonance in Solids by W. Low (Academic Press, NY 1960) p. 87.

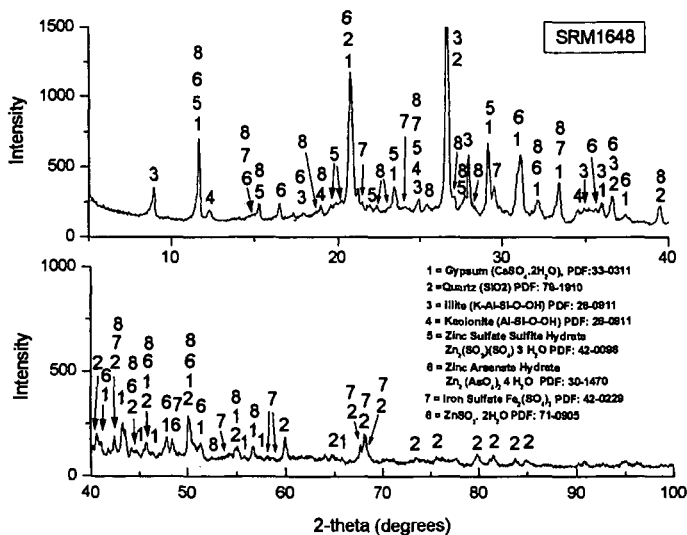


Figure 1. Room temperature x-ray diffractogram of the NIST SRM1648 sample. Lines due to various crystalline components are identified. The broad background near $2\theta \sim 25^\circ$ is due to amorphous carbon.

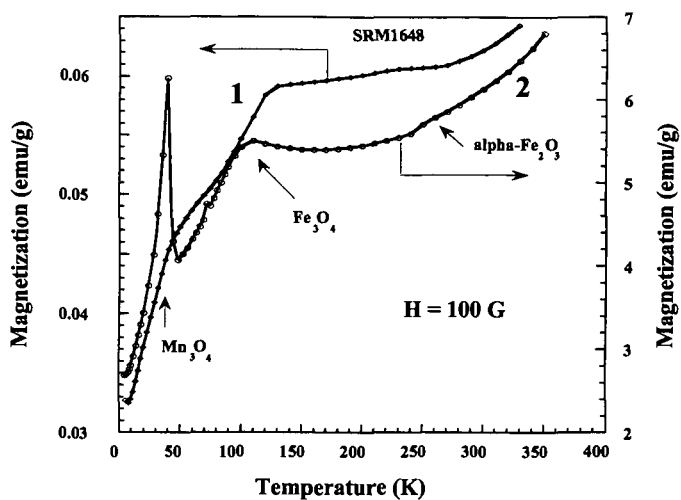


Figure 2. Temperature variation of the magnetization for SRM1648 (data 1) and for a laboratory prepared mixture of Fe_3O_4 , Mn_3O_4 and $\alpha\text{-Fe}_2\text{O}_3$ (1:1:1) (data 2). The transition temperatures indicated by arrows observed for the mixture are also observed in SRM1648.

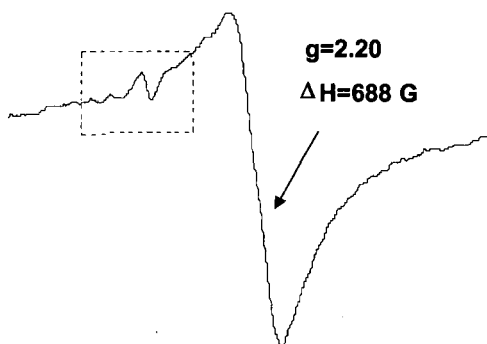


Figure 3. Room temperature ESR spectrum of SRM1648. The line shown by arrow at $g = 2.2$ is probably due to ferrimagnetic Fe_3O_4 .

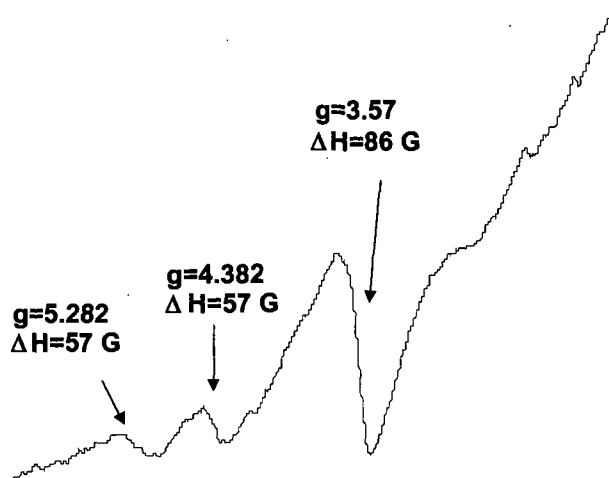


Figure 4. Expanded ESR spectrum of the box area shown in Figure 3. For some of the lines g and ΔH values are indicated. See text for details.